Title

Subevents of long-period seismicity: Implications for hydrothermal dynamics during the 2004-2008 eruption of Mount St. Helens

Journal

Journal of Geophysical Research, 115(B12)

ISSN

0148-0227

Authors

Matoza, Robin S
Chouet, Bernard A

Publication Date

2010-12-14

DOI

10.1029/2010JB007839

Peer reviewed

Subevents of long-period seismicity: Implications for hydrothermal dynamics during the 2004–2008 eruption of Mount St. Helens

Robin S. Matoza[1,2] and Bernard A. Chouet[3]

Received 11 July 2010; revised 1 September 2010; accepted 15 September 2010; published 14 December 2010.

[1] One of the most striking aspects of seismicity during the 2004–2008 eruption of Mount St. Helens (MSH) was the precise regularity in occurrence of repetitive long-period (LP) or "drumbeat" events over sustained time periods. However, this precise regularity was not always observed, and at times the temporal occurrence of LP events became more random. In addition, accompanying the dominant LP class of events during the 2004–2008 MSH eruption, there was a near-continuous, randomly occurring series of smaller seismic events. These *subevents* are not always simply small-amplitude versions of the dominant LP class of events but appear instead to result from a separate random process only loosely coupled to the main LP source mechanism. We present an analysis of the interevent time and amplitude distributions of the subevents, using waveform cross correlation to separate LP events from the subevents. We also discuss seismic tremor that accompanied the 8 March 2005 phreatic explosion event at MSH. This tremor consists of a rapid succession of LPs and subevents triggered during the explosion, in addition to broadband noise from the sustained degassing. Immediately afterward, seismicity returned to the pre-explosion occurrence pattern. This triggering in relation to the rapid ejection of steam from the system, and subsequent return to pre-explosion seismicity, suggests that both seismic event types originated in a region of the subsurface hydrothermal system that was (1) in contact with the reservoir feeding the 8 March 2005 phreatic explosion but (2) not destroyed or drained by the explosion event. Finally, we discuss possible thermodynamic conditions in a pressurized hydrothermal crack that could give rise to seismicity. Pressure drop estimates for typical LP events are not generally large enough to perturb pure water in a shallow hydrothermal crack into an unstable state. However, dissolved volatiles such as CO_2 may lead to a more unstable system, increasing the seismogenic potential of a hydrothermal crack subject to rapid heat flux. The interaction of hydrothermal and magmatic systems beneath MSH in 2004–2008 thus appears able to explain a wide range of observed phenomena, including subevents, LP events, larger ($M_d > 2$) events, and phreatic explosions.

Citation: Matoza, R. S., and B. A. Chouet (2010), Subevents of long-period seismicity: Implications for hydrothermal dynamics during the 2004–2008 eruption of Mount St. Helens, *J. Geophys. Res.*, *115*, B12206, doi:10.1029/2010JB007839.

1. Introduction

[2] The escalation of long-period (0.5–5 Hz) seismicity at shallow depth (<2 km) in a volcanic edifice is often explained in terms of the pressure-induced disruption of a shallow hydrothermal region, and is therefore one of the most significant indicators of volcanic unrest [*Chouet et al.*, 1994; *Chouet*, 1996a]. Long-period (LP) seismicity includes individual LP events and tremor. LP events are transient, volumetric signals characterized by a short-lived (~10 s) broadband onset, followed by a coda of decaying harmonic oscillations lasting from tens of seconds to a few minutes in duration [*Chouet*, 1996a]. Tremor is a more continuous vibration of the ground with observed durations of minutes to hours, or even weeks to years in some cases [*McNutt*, 1992]. Although observations of volcanic tremor are multifarious and tremor probably results from a variety of fluid processes [*McNutt*, 1992; *Chouet*, 1996b], in many instances LP events and tremor have similar spectral properties. This leads to the interpretation that LP events represent the impulse response of a resonant tremor-generating system, and that some types of tremor consist of the superposition of many individual LP events [*Latter*, 1979; *Fehler and Chouet*, 1982; *Fehler*, 1983; *Chouet*, 1985].

[3] Seismic unrest began at Mount St. Helens (MSH) on 23 September 2004, after a month of abnormally high rainfall [*Scott et al.*, 2008], with a swarm of shallow (<2 km) volcano-

[1]Institute of Geophysics and Planetary Physics, Scripps Institution of Oceanography, La Jolla, California, USA.
[2]Now at CEA/DAM/DIF, Arpajon, France.
[3]U.S. Geological Survey, Menlo Park, California, USA.

0148-0227/10/2010JB007839

tectonic (VT) earthquakes that increased in intensity on 25 September 2004 [*Dzurisin et al.*, 2005; *Moran et al.*, 2008a]. Between 27 September and 5 October 2004 these VTs were gradually replaced by a regular occurrence of events with lower dominant frequencies and long-duration codas [*Moran et al.*, 2008a]. This increase in seismicity culminated in tremor on 2 and 3 October 2004, and a series of small (Volcanic Explosivity Index ~1) phreatic explosions on 1, 3, 4, and 5 October 2004. The sequence of seismic events then continued, albeit with variability in amplitude, spectral and temporal characteristics, for over 3 years before finally waning in January 2008. During this time only two phreatic explosions occurred (on 16 January 2005 and 8 March 2005 [*Moran et al.*, 2008b]). This long sequence of seismic events at MSH was characterized by highly repetitive yet slowly evolving waveforms [*Moran et al.*, 2008a; *Thelen et al.*, 2008; *Waite et al.*, 2008], indicating the repeated action of a nondestructive source process with a source time function or source location that evolved slowly as a function of time. In addition, at times during 2004–2008, the events occurred with such regularity (near-constant interevent time spacing) that they were termed *drumbeats* [*Moran et al.*, 2008a].

[4] Different explanations have been offered for the origin of this sustained sequence of repetitive events. The 2004–2008 MSH eruption was characterized by extrusion of solid dacite spines mantled by gouge zones ~1–3 m thick consisting of cataclasite, breccia and unconsolidated gouge, and marked by multiple slickensides [*Pallister et al.*, 2008a; *Cashman et al.*, 2008], which suggested qualitatively a shear faulting source process [*Iverson et al.*, 2006; *Harrington and Brodsky*, 2007; *Moran et al.*, 2008a]. *Iverson et al.* [2006] suggested that each drumbeat event corresponds to an individual stick-slip motion of the solid lava plug and that the repetitive nature of the drumbeat events is related to extrusion dynamics of the solid plug forced upward by more molten magma at depth in the conduit. In this stick-slip model, the long-duration coda of the observed seismic events would be explained by path effects, such as seismic waves trapped in near-surface weathered layers [*Malone*, 1983; *Goldstein and Chouet*, 1994].

[5] However, such a shear faulting source process is inconsistent with many observations. Firstly, investigators were unable to capture stick-slip motions of the lava spines geodetically (D. Dzurisin, Cascades Volcano Observatory, U. S. Geological Survey, personal communication, 2007), and correlation between spine extrusion rate and seismicity rate was at times poor [*Moran et al.*, 2008a]. Secondly, analysis of the seismic events as recorded on a dense network of 19 three-component broadband seismometers by *Waite et al.* [2008] revealed that they had all-dilatational first motions where visible. The stick-slip source mechanism of *Iverson et al.* [2006] would be represented by a combination of a double-couple moment tensor associated with shearing of highly viscous magma at the conduit wall, and a reaction force resulting from sudden acceleration of the lava spine. If a near-vertical single force were to dominate the proposed stick-slip mechanism (assuming near-vertical acceleration of the spine), an upward acceleration of the spine could result in downward first motions everywhere on the network. However, *Waite et al.* [2008] also performed full waveform inversion and obtained a source mechanism consisting of a volume change combined with a vertical single force component. Both of these components had long-duration and oscillatory source time functions. In addition, the seismic events were found to have common spectral peaks observed on stations at multiple azimuths and ranges from the source, which is indicative of source rather than path resonance. These are all defining characteristics of LP events. For these reasons, and following the classification system of *Lahr et al.* [1994], we refer to these seismic events as LP events. We further note that the highly repetitive and regular nature of the seismic events is typical of LP events as observed at numerous volcanoes worldwide [e.g., *Ramos et al.*, 1999; *Stephens and Chouet*, 2001; *Green and Neuberg*, 2006; *Petersen*, 2007].

[6] Atmospheric acoustic (infrasound) observations were also consistent with a source process for the seismic events involving fluids [*Matoza et al.*, 2009b]. *Matoza et al.* [2009b] showed that MSH LP events during 2004–2005 were at times accompanied by impulsive, broadband infrasound signals, and found that these signals could not be explained by simple seismic-acoustic wave conversion. They proposed rapid fluid expansions into loosely consolidated shallow subsurface rock layers as an explanation for the infrasound signals.

[7] The point source inversions of *Waite et al.* [2008] imaged a composite of a volumetric moment tensor and a vertical single force source at a depth of ~200 m ± 200 m below the 1980s crater floor. The volumetric moment tensor had diagonal elements in the ratio M_{xx}:M_{yy}:M_{zz} ~ 1:1:3, which can be interpreted as the volumetric motion of a sub-horizontal, fluid-filled crack, whereas the vertical single force component can be interpreted as small vertical elastic oscillations of the rock mass perched above the crack. Attenuation in the fluid-crack system was investigated by application of the Sompi method [*Nakano et al.*, 1998] to the LP events, resulting in growth rates corresponding to Q of 10–20 [*Waite et al.*, 2008], which can be attributed to bubbly magma, bubbly water, or steam [*Kumagai and Chouet*, 2000; *Kumagai et al.*, 2005]. We note that this range of Q is inconsistent with resonance in the viscous magma column underlying the solid lava plug. Bubbly magma at shallow depth (<1 km) is unlikely at MSH, but water and steam are probably in abundant supply.

[8] An active hydrothermal system is indicated at MSH by the emergence of hot water, rich in minerals and magmatic volatiles, from springs and seeps in the vicinity of Loowit Creek and Step Creek in The Breach [*Shevenell and Goff*, 1993; *Bergfeld et al.*, 2008], which is the area to the north of the MSH crater exposed by the 18 May 1980 lateral blast [e.g., *Kieffer*, 1981]. These springs and seeps, present since 1983, are believed to represent limited discharge of water from beneath the crater area, from both juvenile and meteoric sources [*Shevenell and Goff*, 1993]. Until at least 1998, continuous fumerolic activity also occurred at the 1980–1986 lava dome, but by 2002 only diffuse steam was observed from this area [*Bergfeld et al.*, 2008]. Recent self-potential (SP) and time domain electromagnetic (TEM) data have also pointed to a shallow hydrothermal system that was persistent throughout the 2004–2008 MSH eruption, and was not boiled off by magmatic heating [*Bedrosian et al.*, 2007, 2008]. *Bedrosian et al.* [2007] attributed a strong dipolar SP anomaly in the MSH crater to a hydrothermal circulation cell consisting of a central upward flow of water vapor near the 1980–1986 lava dome from a magmatic source at depth,

combined with a downward flow of water along the flanks of the dome after the rising vapor had condensed at shallow depth. *Bedrosian et al.* [2008] further proposed that a conductor at ~80 m depth imaged in 2007 by the TEM method can be explained by a perched aquifer above an andesitic flow of the Castle Creek sequence (2,200–1,700 years ago), while a conductor at ~250–290 m depth may represent a deeper aquifer within either the Castle Creek sequence or possibly the underlying Pine Creek sequence (3,000–2,500 years ago). This evidence for a stable and persistent hydrothermal system within a few hundred meters of the 1980s crater floor is qualitatively consistent with the LP source process envisioned by *Waite et al.* [2008].

[9] *Waite et al.* [2008] proposed that the subhorizontal crack imaged in the moment tensor inversions at ~200 m ± 200 m depth consists of a water- or steam-filled crack, maintained at high heat and pressure by magmatic activity. Intermittently, pressure in the crack exceeds the containment pressure of a "valve" sealing the crack, leading to rapid collapse of the crack (the "trigger" of the LP event) and resonance of the remaining fluid (the coda of the LP event). To explain the all-dilatational first motions, the initial rupture of the valve sealing the crack is considered a relatively aseismic process in comparison to the coincident volumetric collapse. *Matoza et al.* [2009b] proposed that this model can also explain impulsive infrasonic signals associated with the LP events, where the sudden failure of the valve results in a rapid fluid expansion, propagating the trigger signal into the atmosphere through shallow porous and permeable weathered material overlying the source. In this model, the regular interevent time spacing between individual LP events corresponds to the time taken for fluid pressure and temperature conditions in the crack to recharge back to the critical conditions for valve failure.

[10] A critical requirement for proposed source mechanisms of LPs at MSH is that the source processes are seismogenic, and can produce the observed amplitudes of seismic waveforms. For instance, shear textures in rock such as slickensides and fault gouge can be generated aseismically by slow frictional movement along faults without generating seismic energy [*Scholz*, 2002], so the existence of the gouge zone features is not proof in itself that shear faulting is the seismic source. Furthermore, the seismic moments and single forces predicted by shear faulting appear to be too small to produce the observed range in LP seismic amplitudes at MSH. The magnitudes of volumetric moments and vertical single force components for the LP events obtained by *Waite et al.* [2008] are up to 2×10^{13} N m and 8×10^{9} N, respectively. In contrast, *Iverson et al.* [2006] obtained a force of $\sim 7 \times 10^{7}$ N for a slip of 5 mm, which is 2 orders of magnitude smaller than the single force obtained by *Waite et al.* [2008]. Direct estimates of the seismic moment ($M_0 = \mu dA$, where μ is the shear modulus, d is the slip on a fault, and A is the area of the rupture) can also be attempted using field observations of the fault surfaces on MSH lava spines by *Pallister et al.* [2008b]. The fracturing on the lava spines is evident at multiple scales, ranging from meter-scale Riedel shears to micron-scale fractures within the fault gouge [*Pallister et al.*, 2008b]. However, assuming a representative fault area of ~440 m^2 and a slip of ~4 mm, *Pallister et al.* [2008b] obtained estimates of $M_0 \sim 10^{9}$–10^{10} N m, which is 3–4 orders of magnitude smaller than the moment obtained by *Waite et al.* [2008]. These considerations suggest that the observed shear faulting may not be a powerful enough source to produce the dominant class of LP events observed throughout the 2004–2008 MSH eruption, but could potentially generate lower-amplitude seismicity.

[11] This paper presents seismic observations that are of critical importance to models of seismogenesis at MSH. We show that, accompanying the dominant LP class of events during the 2004–2008 MSH eruption, there is a near-continuous, randomly occurring series of smaller seismic events. These *subevents* are most clearly observable at stations deployed in or close to the MSH crater, i.e., in the immediate vicinity of the LP seismic source region [*Waite et al.*, 2008]. The subevents are not always simply small-amplitude versions of the dominant LP class of events, but appear instead to result from a separate, random process only loosely coupled to the main LP source mechanism. The subevents have amplitudes in the range of applicability of shear faulting [*Tuffen and Dingwell*, 2005; *Iverson et al.*, 2006; *Pallister et al.*, 2008b], hence a detailed analysis of their characteristics is important. LP events at other volcanoes have also been accompanied by subevents, however, in most reported instances, the subevents may be considered a coupled precursor with a more consistent time delay in relation to the LP event [e.g., *Gil Cruz and Chouet*, 1997; *Caplan-Auerbach and Petersen*, 2005]. In addition, the source mechanism of these subevents has not been considered in any significant detail [*Caplan-Auerbach and Petersen*, 2005].

[12] We present an analysis of the amplitude and interevent time distributions of both LPs and subevents at MSH, and investigate the relationship between LPs and subevents using waveform cross correlation. We also discuss the seismic tremor that accompanied the 8 March 2005 phreatic explosion event at MSH. This tremor consists of a rapid succession of LPs and subevents triggered during the explosion, in addition to broadband noise from the sustained degassing. This triggering in relation to the rapid ejection of steam from the system suggests that both seismic event types originated in the subsurface hydrothermal system. Finally, we comment on the source processes possible in a shallow hydrothermal system due to the thermodynamic properties of water with dissolved volatiles, and show that subevents and LP events may both reflect slightly different aspects of the dynamics of a pressurized subsurface hydrothermal system.

2. Data

2.1. Seismic Stations

[13] Figure 1 shows a map of seismic stations used in this study. Station BLIS was an accelerometer deployed by helicopter on a "spider" platform for near-field seismic monitoring [*LaHusen et al.*, 2008; *McChesney et al.*, 2008]. The location of this station is optimal for recording very small amplitude seismic events within the MSH crater, i.e., within the epicentral region of the LP source (Figure 1). However, the response of this short-period accelerometer is peaked at ~18 Hz, and rolls off sharply toward low frequencies. This makes BLIS suitable for assessing timing and relative amplitude and waveform information, but not for the purposes of quantitative waveform or spectral analysis. In particular, the extended resonance coda of the MSH LP events is not well recorded at BLIS due to the instrument response,

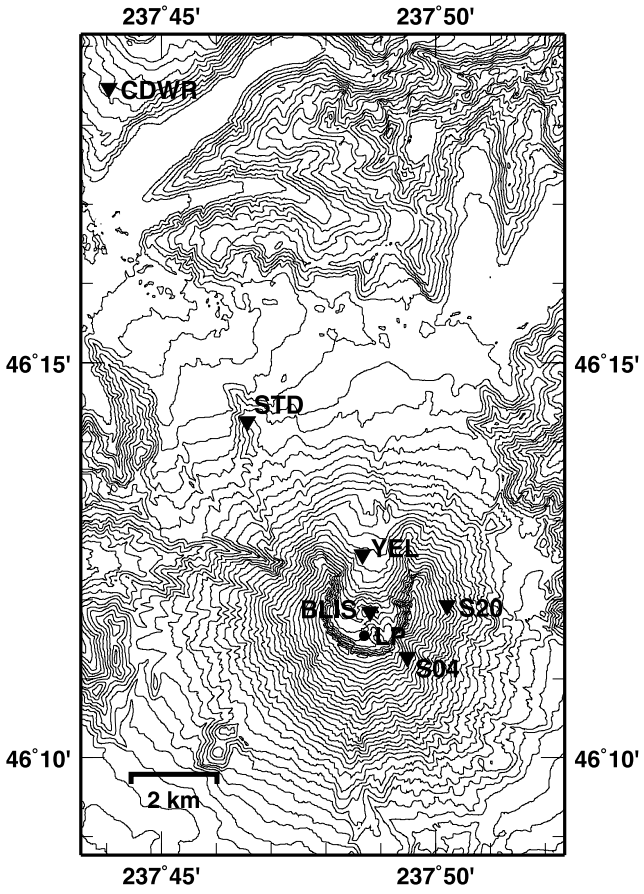

Figure 1. Map of seismic stations (inverted solid triangles) used in this study. The LP source location of *Waite et al.* [2008] is indicated by the solid dot labeled "LP." Contour interval is 50 m. The seismic stations shown represent only a small subset of the total seismic network used to monitor Mount St. Helens [*Moran et al.*, 2008a].

and only the higher-frequency trigger components are recorded. For this reason, we use raw counts as amplitude units for BLIS throughout this study. We therefore use BLIS for analysis of the relative amplitude and interevent time distributions for seismicity, while grounding these observations with data from broadband stations S04, S20 [*Waite et al.*, 2008], STD [*Moran et al.*, 2008a] and CDWR [*Matoza et al.*, 2009b], and short-period station YEL [*Moran et al.*, 2008a]. The periods of data availability do not always overlap for these stations. For instance, BLIS was deployed in early October 2004, but was destroyed in January 2005, while data from broadband stations S04 and S20 are only available after 21 June 2005. Nevertheless, by using YEL, STD and CDWR it is possible to correlate observations at the various stations to some extent.

2.2. Subevents

[14] Figure 2 shows examples of waveforms recorded at S04 that are typical of those recorded throughout the 2004–2008 MSH eruption at stations in the vicinity of the crater. In Figure 2a (data from 20 October 2005), four repetitive LP events are recorded with almost identical waveforms and some variability in their amplitude, with a fairly regular interevent time. In addition, we can identify three events with smaller amplitude (indicated by vertical arrows) that occur in the time intervals between the four main LP events. *Moran et al.* [2008a] also noted that these small earthquakes were recorded on stations inside the crater during 2004–2005 and that they are not drumbeats (LPs). In particular, these events did not occur with the regular interevent time spacing that was characteristic of drumbeat events. We refer to these events with smaller amplitude as *subevents* that are occurring within the LP seismicity. It is clear from Figure 2a that the subevents do not occur with a consistent time delay in relation to the main LP events, and we note that the first LP event in this sequence is not immediately preceded or followed by any subevent. From Figure 2a we may also hypothesize that the overall event amplitude distribution for seismicity at MSH may be bimodal, with one peak at larger amplitudes corresponding to the typical LP events, and another peak at lower amplitudes corresponding to the subevents.

[15] However, Figure 2b shows another sequence of data from the same station on 9 November 2005. During this time period, we see a similar pattern of repetitive LP seismic events accompanied by subevents, but the amplitude distribution of the overall seismicity is less clear. For example, the event beginning at ~175 s has an intermediate amplitude, and classification of this event as either LP or subevent would be arbitrary at this stage. In section 3, we provide a more formal discussion of the amplitude distribution of seismicity at MSH, and show that separation of LP events and subevents can be better performed via waveform cross correlation. Figure 2b also includes a spectrogram showing the frequency content of the LPs and subevents as a function of time. Despite their lower signal power, the subevents commonly have frequencies within the same range as the typical LP events. Long-duration codas can be observed in the spectrogram for several of the subevents. Figure S1 shows a record section of the events shown in Figure 2b.[1] Figure S1 shows that the subevents shown in Figure 2b can be observed above noise at least as far as ~4.5 km from the LP epicenter during this time period.

2.3. Triggering of LPs and Subevents During the 8 March 2005 Phreatic Explosion

[16] The occurrence of subevents within LP seismicity was particularly prominent during the 8 March 2005 phreatic explosion at MSH. LP event amplitudes increased ~2 hours prior to the explosion, resulting in an increase in RSAM (Real-Time Seismic Amplitude Measurement) values. However, no other attributes of the steady state LP event sequence such as number of events per unit time, event type, frequency content, event location, or event waveforms changed significantly prior to this explosion [*Moran et al.*, 2008b]. Instead, the steady state occurrence of LP drumbeat events that had been occurring for the previous 5 months was suddenly punctuated by tremor associated with the explosion (Figure 3). The increase in LP event amplitudes and RSAM values prior to the phreatic explosion may be attributed to increased pressurization in the system prior to the explosive release. The characteristics of the seismic tremor recorded during the explosion

[1] Auxiliary materials are available in the HTML. doi:10.1029/2010JB007839.

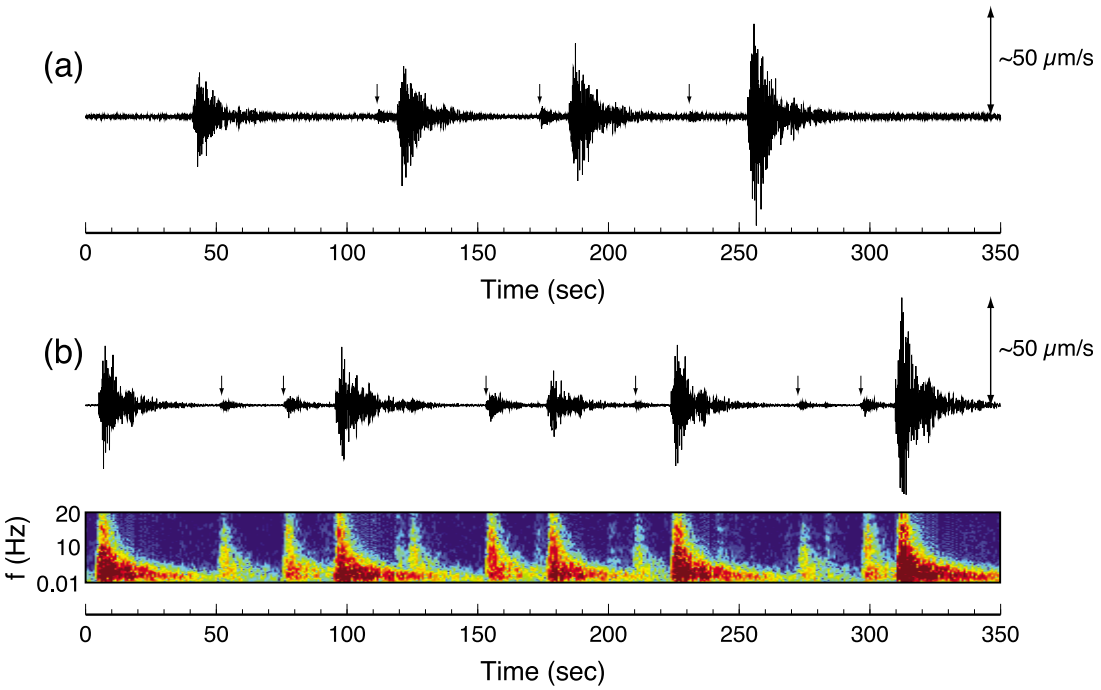

Figure 2. Waveforms at S04 showing typical examples of LP events and subevents (indicated by arrows) at MSH: (a) origin time 1541:43 UTC, 20 October 2005; (b) origin time 2152:37 UTC, 9 November 2005. Waveforms in Figure 2b are accompanied by a corresponding spectrogram (frequency axis linear from 0.01 to 20 Hz). Note in the spectrogram that two subevents are buried within the coda of an LP event between 100 and 150 s.

can be better understood by reference to simultaneous infrasound data [*Matoza et al.*, 2007]. Large-amplitude, broadband infrasonic tremor is recorded during sustained vulcanian and plinian degassing, providing the exact timing and duration of turbulent fluid flow in the atmosphere (top trace, Figure 3b) [*Matoza et al.*, 2007, 2009a]. The seismic data during this event consist of the steady state sequence of regular LP events prior to the explosion, tremor during the explosion, and the rapid return to the pre-explosion steady state occurrence pattern immediately following the explosion (seismic traces, Figure 3b). Thus, the LP source was not destroyed during the explosion.

[17] The seismic tremor consists of two main components: (1) a broadband eruption tremor component with an amplitude envelope mimicking the infrasonic tremor signal and (2) a spasmodic tremor consisting of a rapid succession of triggered LPs and subevents. The first component is most clearly seen in seismic data filtered 5–15 Hz (third trace from top, Figure 3b), as this component is dominant in this frequency band. The second component can be seen in the data filtered 1–5 Hz, as this is the band of the LP events.

[18] We note that the infrasonic trace in Figure 3a has been time advanced by 38 s, the approximate time delay between seismic and acoustic signals sourced simultaneously at MSH as recorded at CDWR. Since the time-advanced infrasonic tremor signal begins ~45 s following the onset of the seismic tremor signal (that is, the infrasonic signal arrived at CDWR ~45 + 38 = 83 s after the seismic signal arrived (Figure 3a)), we can conclude that the broadband component of the seismic tremor does not simply represent air-ground coupling of the broadband infrasonic tremor signal. Instead, the broadband component of the seismic tremor signal probably represents

Figure 3. Waveforms during the 8 March 2005 phreatic explosion at MSH. (a and c) Expanded views of data indicated by boxes in (b). See Figure 1 for location of stations CDWR, STD, and YEL. Channel names: BDF, broadband infrasound data; BHZ, broadband vertical seismic data; EHZ, short-period vertical seismic data (high-gain). The data are shown filtered in various frequency bands (indicated at left, YEL unfiltered). Infrasound data (BDF) have been time advanced 38 s to correct for seismic-acoustic time delay at CDWR. The 8 March 2005 phreatic explosion is delineated by a large-amplitude broadband infrasonic signal ("J" marks onset) between ~1575 and 4740 s, which represents the turbulent flow of erupted material in the atmosphere [*Matoza et al.*, 2009a]. In the seismic data prior to the explosion (Figure 3a), LP events occur with regular interevent time spacing, and subevents are visible at YEL (arrows). During the explosion (Figure 3b), the seismic waveforms consist of a superposition of (1) broadband eruption tremor most clearly visible in CDWR 5–15 Hz filtered BHZ data (duration coincides approximately with infrasound signal) and (2) a sequence of LPs and subevents triggered rapidly during the explosion. Figure 3c shows a time during the explosion after the broadband eruption tremor signal has decreased in amplitude, enabling clear recording of the triggered LP and subevent (arrows) sequence during the explosion. After the explosion, LP seismicity returns to the steady state, regular drumbeat pattern.

the rapid disturbance of the subsurface reservoir containing the fluid erupted during this explosion, the turbulent ascent of the fluid through near-surface vents toward the atmosphere, and some limited air-ground coupling of the infrasound signal that occurred once fluid entered the atmosphere.

[19] The second, spasmodic, component of the seismic tremor is best viewed in Figure 3c, which depicts a time during the seismic tremor when the amplitude of the broadband component has decreased (see 5–15 Hz filtered data from CDWR (Figure 3b)). During this time, the spasmodic

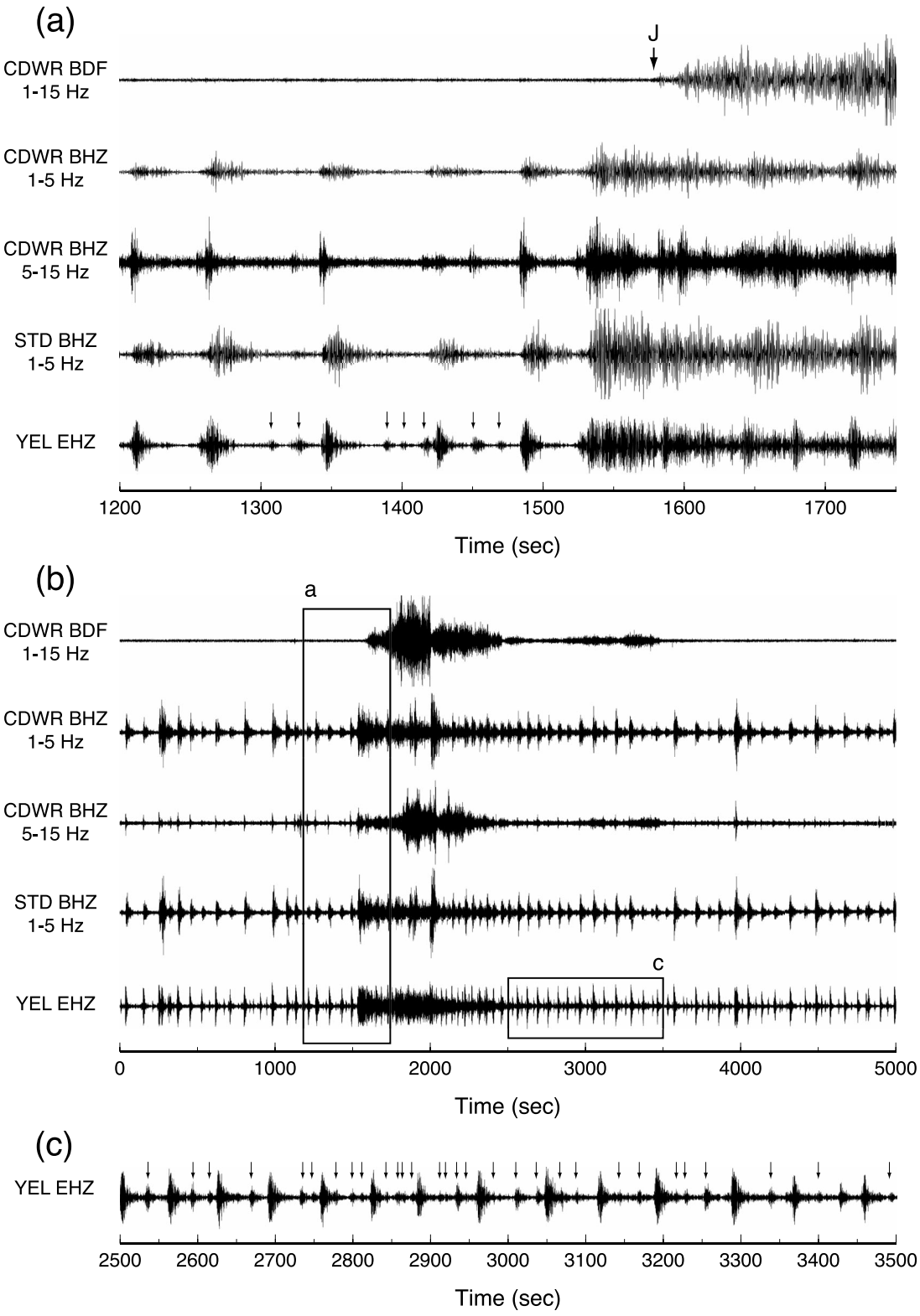

Figure 3

tremor consisting of LPs and subevents has higher amplitude than the broadband tremor component. In Figure 3c we see that this spasmodic tremor consists of a sequence of rapidly triggered LP events and a large number of subevents. The data from YEL (Figure 3a) indicate that the broadband tremor component dominates the record in the first minutes of the tremor. The implications of this 8 March 2005 sequence for the LP and subevent source mechanism at MSH are discussed in sections 5.2 and 6.

3. Analysis of Amplitude and Interevent Time Distribution

[20] One of the most striking aspects of seismicity during the 2004–2008 eruption of MSH was the precise regularity in occurrence of repetitive LP events over sustained time periods (i.e., drumbeats). However, this repetitive interevent time was not always observed, and at times during the eruption the temporal occurrence of LP events became more random. An analysis of MSH drumbeat interevent time spacing was performed by *Moran et al.* [2008a], who found that it did not change significantly between 16 October 2004 and 11 April 2005. Between April and July 2005, event spacing gradually increased and then became more random, but regularity (repetitive interevent time spacing) returned by October 2005. In this study we investigate the amplitude distribution and interevent time spacing of seismicity at MSH during isolated time periods during the 2004–2008 eruption. We first focus on the time interval 4–16 November 2004 (sections 3 and 4) as this represents a time early in the 2004–2008 eruption when a regular interevent time for LP events (or drumbeating) was well defined. We show that during 4–16 November 2004, subevents accompanying the regular drumbeat LP occurrence are well described by a Poisson process. In section 5, we focus on times when multiple, high-quality broadband seismic stations were available. We study the time from 18 October to 24 December 2005 as this represents a time when drumbeating of LP events returned after several months of more irregular interevent times [*Moran et al.*, 2008a]. Finally, we also study 1–31 July 2005 which represents a time when the temporal occurrence of LP events was somewhat more random [*Moran et al.*, 2008a].

3.1. Automatic Event Picking

[21] Event picking was performed using an STA/LTA detector with parameters adapted at each station to observed differences in event amplitudes, signal-to-noise ratio, and coda duration. At BLIS we used the vertical component of acceleration filtered between 0.5–10 Hz with STA length: 0.5 s, LTA length: 5 s, and STA/LTA ratio for detection: 1.75. At S04 and S20 we used the vertical component of velocity filtered between 0.5–10 Hz with STA length: 0.5 s, LTA length: 5 s, and STA/LTA ratio for detection: 3. The detection threshold was set conservatively to achieve a low number of false detections. Furthermore, the STA/LTA algorithm has a finite time resolution for triggering events. Events with interevent time spacing on the order of the STA length are not detected as separate events. An examination of the waveform data indicates that such very short time spacings exist for some subevents, and occasionally the time spacing is so short that the events would be better described as a short-lived tremor. We show that these short-lived tremors may be viewed as the end-members of a Poisson process describing the subevents, since short interevent times occur with the highest probability in the exponential distribution.

3.2. Amplitude Distribution

[22] Figure 4a shows a scatterplot of amplitudes for the 42,426 events detected at BLIS between 4 and 16 November 2004. The amplitudes correspond to the peak amplitude of STA/LTA detections in the 0.5–10 Hz band. The density of points in this scatterplot forms a bimodal distribution in amplitude throughout this time period. Figure 4b shows more clearly the density distribution of points in the scatterplot (Figure 4a), and the nonstationarity in the event amplitude distribution as a function of time. Events with amplitude less than 15 counts (below horizontal white line) maintain a fairly constant amplitude distribution during this time period, while events with amplitude greater than 15 counts (above horizontal white line) exhibit slow variations in the average event amplitude. For the time being, we neglect this nonstationarity and analyze the global distribution of event amplitudes during this time period.

[23] Figure 5a is a histogram of all event amplitudes at BLIS shown in Figure 4. The event amplitudes in this time period form a smooth bimodal distribution, suggesting that two distinct processes are acting to generate seismicity. One process may be responsible for the peak at ~40 counts, while another is responsible for the peak at ~7 counts. Assuming that the overall bimodal probability density function (PDF) results from two separate PDFs that are superimposed, we then have the problem of separating the overlapping PDFs. We attempt to separate the PDFs in two ways. In the first attempt, we simply define an amplitude threshold of 15 counts (vertical dashed line, Figure 5a) to separate the events. Although this crude criterion does not take into account the overlapping nature of the PDFs, the results provide some preliminary insights, and are presented in section 3.3. Our second attempt utilizes waveform cross correlation to separate the events. This is discussed in section 4.

3.3. Interevent Time Distribution Using Amplitude Threshold

[24] Figure 5b shows the interevent time distribution of all events with amplitude greater than 15 counts (events to the right of vertical dashed line in Figure 5a). The distribution has a clear peak at ~20 s, indicating that events with amplitude greater than 15 counts tend to occur with a modal average recurrence time of 20 s. This is in agreement with the observation of regularly occurring "drumbeat" events, which constitute the majority of events with amplitude greater than 15 counts. In contrast, Figure 5c shows the interevent time distribution of all events with amplitude less than 15 counts (events to the left of vertical dashed line in Figure 5a), corresponding to the subevents. In contrast to Figure 5b, the most common interevent time (or recurrence time) is the shortest one, with longer interevent times occurring with increasingly small probability. This is characteristic of a Poisson process, and suggests that the events with amplitude less than 15 counts are occurring stochastically.

[25] We use a Kolmogorov-Smirnov (KS) test [*Massey*, 1951] to test the hypothesis that the PDF for the interevent

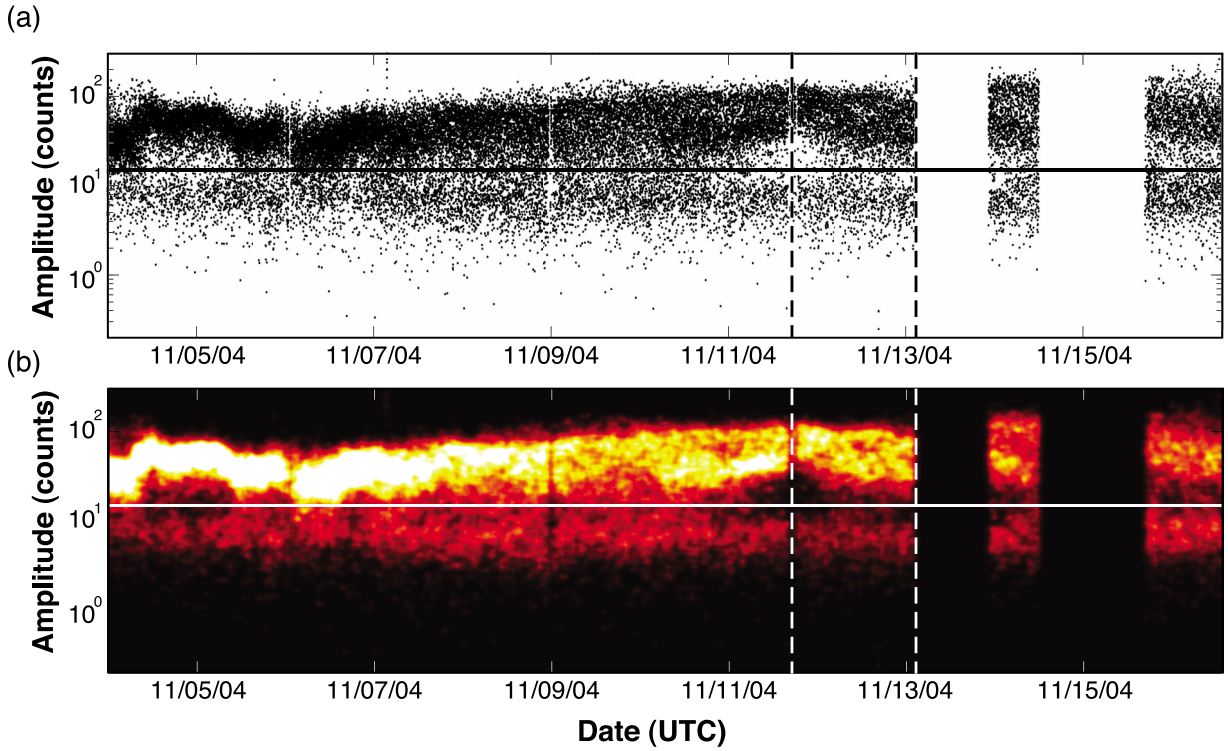

Figure 4. Amplitudes (vertical acceleration in counts, log scale) for all 42,426 events detected at BLIS between 4 and 16 November 2004. (a) Scatterplot: horizontal line indicates amplitude of 15 counts (see Figure 5). Data gaps (e.g., on 13 and 14–15 November 2004) result in outliers in the interevent time distribution, which have been removed from subsequent analysis. Note that the amplitude threshold of 15 counts (horizontal black line) does not completely separate the clusters of larger and smaller events (Figure 5), highlighting the difficulty in separating events on the basis of an amplitude threshold alone. (b) Detection density, showing same data as Figure 4a but converted to a shaded color image to better illustrate the distribution of points. Color scale represents the density of points in the scatterplot (Figure 4a). Black-red-orange-white indicates increasing density of points in the scatterplot (Figure 4a). Vertical dashed lines in both plots indicate time range of data used for initial cross-correlation analysis (section 4, Figures 7 and 8), 1700 UTC on 11 November to 0200 UTC on 13 November 2004.

times of the subevents shown in Figure 5c is Poissonian, i.e., described by an exponential distribution:

$$\phi(x) = \lambda e^{-\lambda x}. \quad (1)$$

The PDF $\phi(x)$ is defined such that the probability of the measured interevent time X lying in the interval $[x, x + \delta x]$ is given by the integral of $\phi(x)$ over $[x, x + \delta x]$. The KS test assumes that we know the rate parameter λ of the exponential distribution we are trying to test against. Since λ is unknown a priori, we perform a grid search over values of λ. For each value of λ, we construct a theoretical exponential cumulative distribution function (TCDF):

$$\Phi(x) = 1 - e^{-\lambda x}. \quad (2)$$

The TCDF $\Phi(x)$ is the probability that an interevent time X will be less than or equal to x. We then apply the KS test to determine whether the data are distributed according to the exponential distribution (equation (2)) with this value of λ. The KS test statistic is the maximum deviation between the empirical cumulative distribution function (ECDF, calculated from the observed interevent times) and Φ [*Massey*, 1951; *Rice*, 1995]. The null hypothesis is that the ECDF is equal to Φ. We perform the KS test with significance level $\alpha = 0.05$. Figure 6a shows the ratio of the p value [*Rice*, 1995] of the KS test to the significance level α, for values of $\mu = \frac{1}{\lambda}$ in the range 85 to 100 s. The p value is interpreted as a measure of the plausibility of the null hypothesis. When the p value is greater than α (i.e., $p/\alpha > 1$), we accept the null hypothesis that the data have an underlying PDF matching our chosen exponential function at the significance level.

[26] We find that the KS test is passed for a range of values of $\mu = \frac{1}{\lambda}$ between ~92.2–93.5 s, and that the optimal fit to the data is obtained for $\mu = \frac{1}{\lambda} \sim 93$ s (Figure 6a). Figure 6b shows the empirical CDF (ECDF) computed from the observed interevent times compared to the theoretical CDF (TCDF) for an exponential distribution with the optimal value of $\mu = 93$ s. Figure 6c shows the difference between the two curves shown in Figure 6b, i.e., TCDF − ECDF. The differences are negligible. The strong agreement between the shapes of the TCDF and ECDF curves provides a further illustration that the data are well described by an exponential distribution with $\mu = 93$ s. This means that the subevents occur randomly in time, but on average one subevent occurs approximately every 93 s.

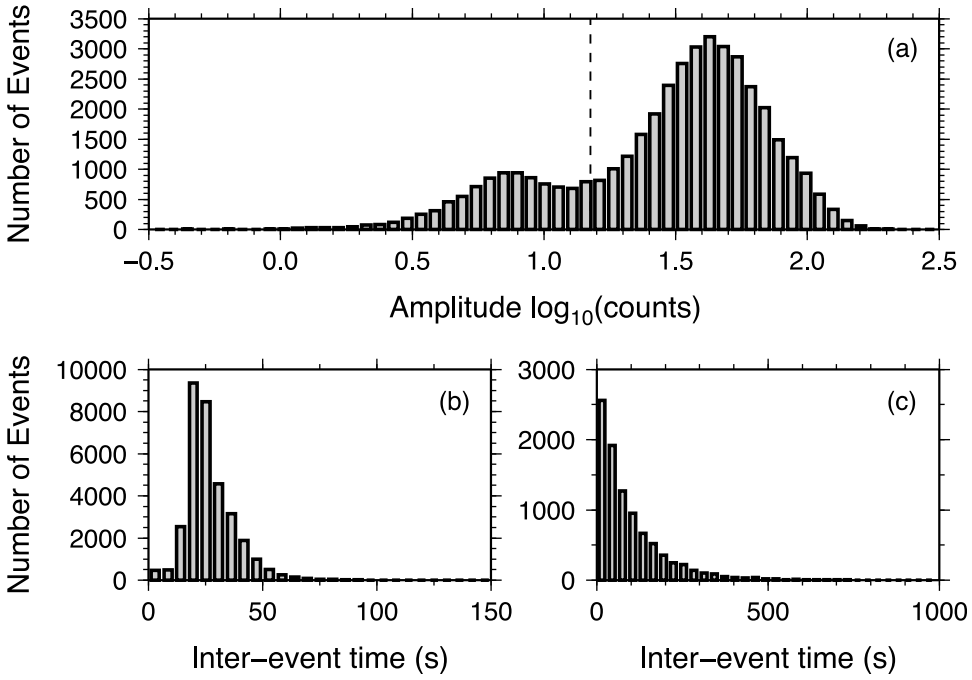

Figure 5. (a) Histogram of event amplitudes ($\log_{10}$ (counts)) for all events detected at BLIS between 4 and 16 November 2004. The 42,426 event amplitudes form a smooth bimodal distribution with one peak centered at ~40 counts ($\log_{10}$(counts) ~ 1.6) corresponding to the "typical" LP events and another peak at ~7 counts ($\log_{10}$(counts) ~ 0.85) corresponding to the subevents. Vertical dashed line indicates value of 15 counts used in preliminary attempt to separate LP events and subevents as shown in (b) and (c). Figure 5b shows a histogram of interevent time (s) for events shown in Figure 5a with amplitude greater than 15 counts (33,114 events). Figure 5c shows a histogram of interevent time (s) for events shown in Figure 5a with amplitude less than 15 counts (9,312 events). Note the difference in time scale between Figure 5b and Figure 5c. The low number of events (9,312) with amplitude <15 counts in comparison to the number of events (33,114) with amplitude >15 counts is partially caused by a sampling bias since lower-amplitude events are more difficult to detect.

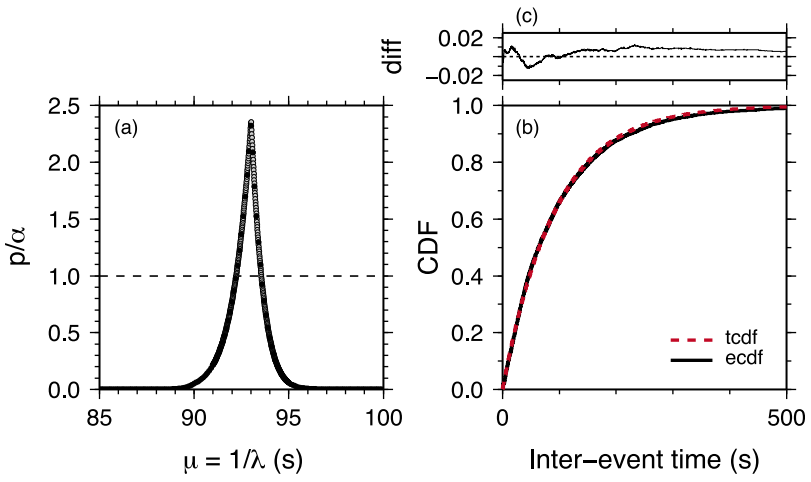

Figure 6. Analysis of the interevent time distribution of subevents (Figure 5c). (a) Results of Kolmogorov-Smirnov (KS) test against theoretical exponential CDFs calculated with different values of λ. When $p/\alpha > 1$, the KS test is passed at the $\alpha = 0.05$ significance level. (b) Comparison of the empirical CDF (ECDF, solid black line) to the theoretical CDF (TCDF, dashed red line) for an exponential distribution with the optimal value of $\mu = 93$ s determined in Figure 6a. (c) Difference between curves shown in Figure 6b, i.e., TCDF − ECDF.

Table 1. Summary of Classification for Three Values of Threshold ψ

Threshold ψ	Total Number of Families	Number of These Families With Only One Event
0.5	16	5
0.6	90	31
0.7	504	321

[27] Taken together, this indicates that the seismicity during 4–16 November 2004 at BLIS consists of (1) "drumbeat" LP events that have greater modal average amplitude and occur regularly with one event every ~20 s and (2) a series of subevents with smaller amplitude that are occurring randomly in time, i.e., not regularly. However, the separation of events based on an amplitude threshold used for this analysis is crude, since the PDFs for amplitude actually overlap (Figure 5a). In section 4 we separate events based on their waveform.

4. Waveform Cross Correlation

[28] Waveform cross correlation has been performed on repetitive LP event sequences at numerous volcanoes [e.g., *Stephens and Chouet*, 2001; *Green and Neuberg*, 2006; *Petersen*, 2007; *Ottemoller*, 2008]. For the 2004–2008 eruption of MSH, waveform cross correlation has been applied to analyze various time periods throughout the 4 year sustained sequence of repetitive LP events [*Thelen et al.*, 2008; *Waite et al.*, 2008; *Matoza et al.*, 2009b]. Here we apply waveform cross correlation to both the typical LP events and subevents. As in previous studies of the 2004–2008 MSH eruption, we only consider isolated time periods from this long sequence of seismic events. LP waveforms and spectral properties gradually evolved, and sometimes changed abruptly, throughout the course of the 2004–2008 eruption [*Moran et al.*, 2008a; *Thelen et al.*, 2008; *Waite et al.*, 2008; *Matoza et al.* 2009b]. A natural extension of the work described in this paper would be to investigate the evolution of the LP and subevent waveform and spectral properties, and amplitude and interevent time distributions throughout the entire 2004–2008 eruption.

[29] Nevertheless, as described in section 3.2, the main motivation behind our waveform classification procedure is to assess whether the bimodal amplitude distribution for seismicity at MSH during 4–16 November 2004 (Figure 5a) can be separated into its two component modes on the basis of event waveform. One mode corresponds to typical LPs, the other corresponds to the subevents. In addition, although it is already known that the LP events have highly repetitive waveforms, it is not known whether the subevents also have repetitive waveforms or are characterized by nonrepetitive waveforms. If the subevents have repetitive waveforms it would imply that, as with LP events, the subevents arise from a rapidly rechargeable, nondestructive source process within a small source volume [*Stephens and Chouet*, 2001]. Alternatively, nonrepetitive waveforms would imply that the subevents result from a more destructive or a more spatially distributed source process. If the subevents have repetitive waveforms, it is also of interest to investigate whether the LPs and subevents have similar or different waveforms in relation to one another. A similar waveform would imply that the subevents represent a low-amplitude end-member of the typical LP class. Alternatively, a different waveform would indicate that the subevents arise from a source location or source time function that is separate from the typical LPs.

4.1. Classification Procedure

[30] We begin our waveform classification procedure by following *Green and Neuberg* [2006]. In this method, we choose a relatively short time period for initial data analysis and cross correlate every single event with every other event in the time period. For n triggered events in the time period, this forms an $n \times n$ matrix $\mathbf{M}$ of maximum correlation coefficient (CC) values, where M_{ij} denotes the maximum CC between events i and j. Here we choose 33 hours from 1700 UTC on 11 November to 0200 UTC on 13 November 2004 for this procedure (Figure 4a), which consists of n = 4295 at station BLIS (Figure 4a). The waveform data were filtered 1–5 Hz, and a 4 s window length was used for the cross correlation. The window length of 4 s was chosen in order to represent individual events with short repeat times accurately. To reduce the computation size, we reduced the sampling frequency to 50 Hz. We found that decimating the data further than this resulted in degraded correlation between similar waveforms due to the waveforms being undersampled.

[31] To sort the correlation matrix $\mathbf{M}$, we define a threshold CC value ψ, and first find the event with the largest number of events correlated with it with CC > ψ [*Green and Neuberg*, 2006]. All of the events corresponding to this first "family" of waveforms are then removed from $\mathbf{M}$ and the process is repeated until all events are sorted into families. This method results in a series of waveform families that are labeled with a family index integer. Family 1 corresponds to the dominant waveform with the largest number of events, and families with increasing index number have fewer and fewer events. The choice of ψ is subjective, and controls both the number of defined event families and the number of unclassified events (Table 1). Unclassified events are events that do not correlate with any other event with CC > ψ. Low values of ψ yield a relatively coarse waveform classification, with only waveforms that are grossly different from one another being grouped into different families. High values of ψ yield a relatively fine classification, where waveforms with subtle differences will be grouped into different waveform families. We found that ψ = 0.6 achieved the best balance (Table 1) and we use this value in all subsequent analysis unless stated otherwise.

4.2. Results of Waveform Classification for 33 h Time Period at BLIS

[32] Figure 7 shows the results of the classification procedure for the 4295 events at BLIS between 1700 UTC on 11 November and 0200 UTC on 13 November 2004. It is instructive to compare this with the results of the previous, more crude, classification based solely on an event amplitude threshold (Figure 4a, section 3.2). We find that the events with amplitude >15 counts (Figure 4a) actually comprise up to ~10 distinct waveform families (Figure 7a). One or two waveform families (family 1, lime green and family 2, orange) are by far the most dominant. Family 1 consists of 2908 events, or ~68% of the events analyzed (Table 2). Family 1 is shown

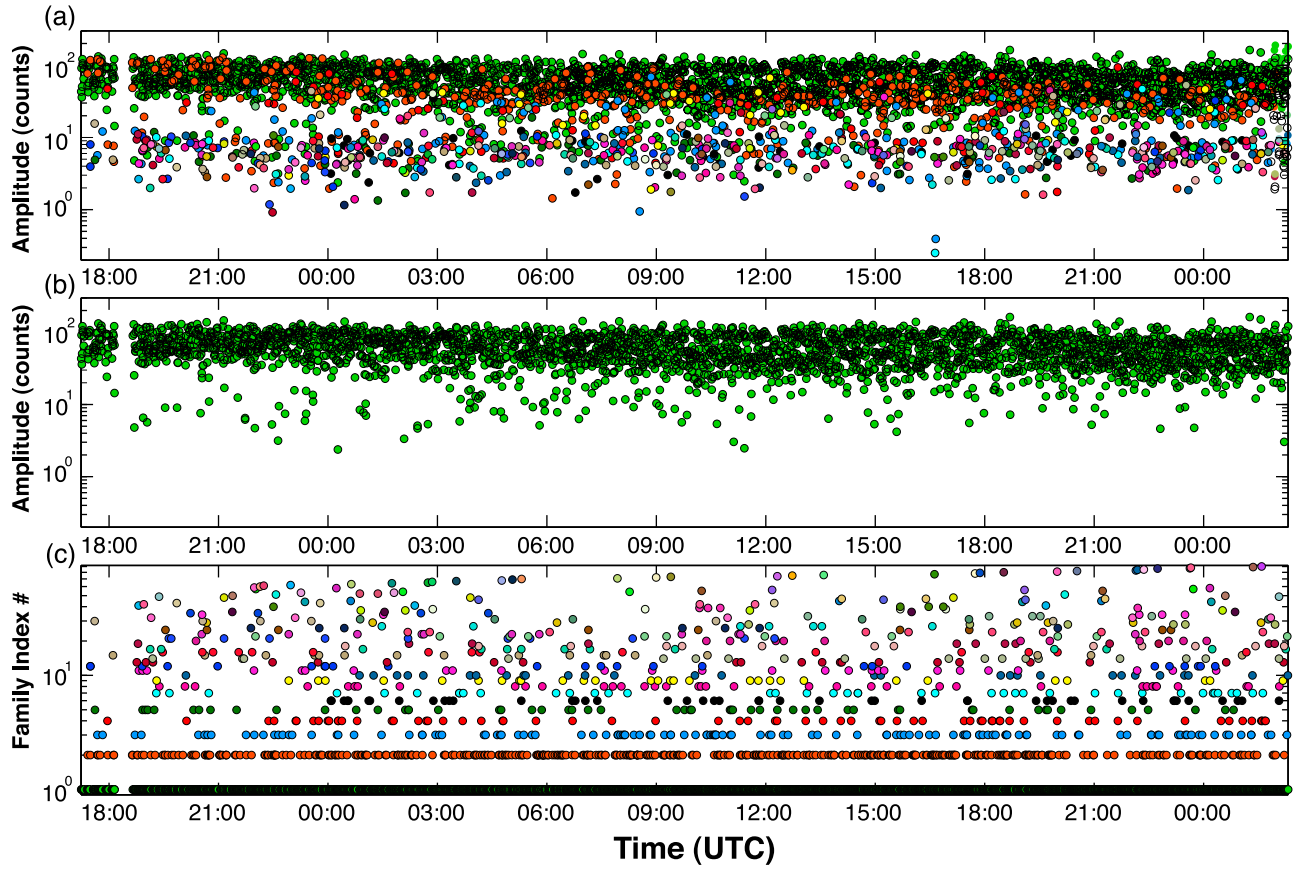

Figure 7. Results of waveform classification for 4295 events occurring between 1700 UTC on 11 November and 0200 UTC on 13 November 2004. (a) Amplitude of event (counts, log scale) versus time and color coded for waveform family index. Compare with Figure 4a where a more crude classification based solely on event amplitude was used. (b) Same as Figure 7a, but only the dominant waveform family (family 1) is shown. (c) Waveform family number (90 families in total) versus time. Family index number is plotted on a log scale to emphasize the lower family index numbers which consist of more events. Families with index number >25 have fewer than 10 events per family, while those with index >60 have only one single event per family (unclassified events) (Table 2). Family 1 (lime green) is the dominant waveform family.

separately in Figure 7b for clarification. We also find that the families making up the majority of events with amplitude >15 counts are also present at lower amplitudes in the subevent category with amplitudes <15 counts. This emphasizes the previous conclusion that the bimodal PDF of all event amplitudes (Figure 5a) represents two separate overlapping PDFs that likely correspond to two distinct source processes. Figure 7 indicates that the two PDFs can be better separated by waveform classification.

[33] In order to evaluate which waveform families correspond to which mode of the PDF shown in Figure 5a, we compute PDFs of the amplitude distribution for various combinations of the waveform families (Figure 8). Since the number of events decreases with increasing family index number (Table 2), we cannot simply compute a PDF of each individual family. The PDFs computed for higher family index numbers would suffer from data undersampling. We therefore compute PDFs for all events with index number ≥q for various values of q ranging from 1 to 10 (solid colored lines, Figure 8). Since families 1 and 2 consist of a large number of events, we also compute the amplitude PDFs for these families individually (black dashed and dashed-dotted lines, Figure 8). When all events are included (green line, q = 1) we obtain a bimodal PDF similar to that observed before (Figure 5a), with a peak between ~40–80 counts ($\log_{10}$[counts] ~ 1.6–1.9) corresponding to the LP events, and a lower peak corresponding to the subevents. We note

Table 2. Number of Events Belonging to Each Family for Classification With ψ = 0.6

Family Index	Number of Events
1	2908
2	457
3	126
4	66
5	55
6	46
7	41
8	37
9	30
>10	<30
>25	<10
>35	<5
60–90	1

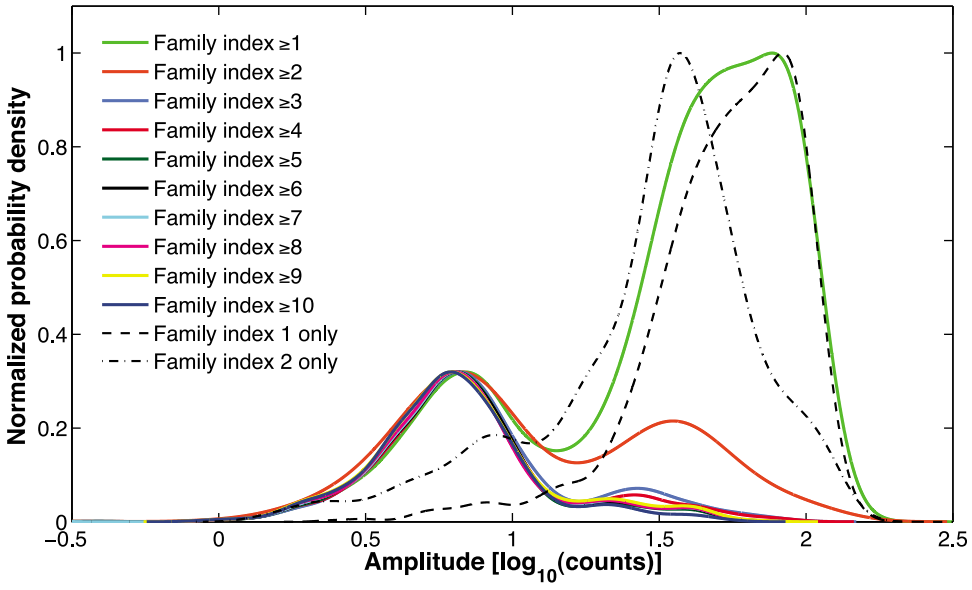

Figure 8. Probability density functions of event amplitude (counts) for various combinations of the event families shown in Figure 7. Colored lines show PDFs of all events in families with index number $\geq q$ where q is varied from 1 to 10. Dashed and dashed-dotted lines show PDFs of individual families 1 and 2, respectively. The PDFs for family index ≥1 (green line) and the PDFs of individual families 1 and 2 (black dashed and dashed-dotted lines) are normalized to their maximum value. All other PDFs normalized to their maximum value and then scaled to second mode at $\log_{10}$(counts) ~ 0.8.

that the distribution shown in Figure 8 does not match the histogram shown in Figure 5a perfectly, in part because the data coverage in Figures 8 and 5a is different.

[34] Upon progressive removal of the dominant waveform families, the PDF changes from being bimodal to unimodal via the progressive disappearance of the peak at ~40–80 counts. This corresponds to stripping away the typical LP events and leaving behind the subevents. In particular, once we remove families 1 and 2 ($q = 3$, light blue line), the peak at ~40–80 counts is largely removed and the PDF is dominated by the subevents. This result is confirmed by the PDFs of the individual event families 1 and 2. The PDFs for these families have dominant peaks at ~40 counts (family 2) and ~80 counts (family 1), and much lower probability at lower event amplitudes. We note that family 2 does have a bimodal distribution (dashed-dotted line), suggesting that the source location and source time function responsible for this family produces both typical LPs and subevents to some degree. This has interesting implications for the dynamics of the source process. In particular, it indicates that the pressure transient or trigger mechanism leading to family 2 can occur at the same location, with the same source time function, with two distinct values of driving pressure (within a broad range) being the most likely.

[35] Another conclusion that can be drawn from this analysis is that the vast majority of subevents, although generally separate from the main LP class of events in both amplitude and waveform type, are repetitive events. This indicates that the subevents also correspond to a rapidly rechargeable, nondestructive source process. In our classification scheme, the subevents constitute ~20 distinct repetitive families, each with at least 10 events. This relatively large number of families in contrast to the ~2 families constituting the LP events may be partially attributed to the lower signal-to-noise ratio of these events, and the consequently degraded correlation between them. It may also indicate that the subevents arise from a relatively distributed source region corresponding to different source locations or varying source time functions. We investigated this by performing further waveform cross correlation between master stacks of the first 10 families. Master stacks were formed by aligning all waveforms in a family and taking the 10% trimmed mean across all waveforms at each time sample. We again used vertical acceleration data at BLIS. We found that the master stacks for families 1 and 2 are correlated with CC = 0.79, indicating that these two families are genetically related. In addition, we found that the master stacks of families 4 and 9 are correlated with families 1 and 2 with CC > 0.6. However, all the remaining event families correlated poorly with families 1, 2, 4 and 9. This indicates that the majority of subevents represent a class of events with separate waveforms from the dominant LP class (i.e., families 1, 2, 4, and 9). Although the genetic relations between different waveform families could be further investigated and developed, this information is not needed for the aims of the current study. We can now separate the dominant LP class (families 1, 2, 4, and 9) from the subevents in longer data segments. This is done simply by extracting all events that correlate with master waveforms from the dominant LP class.

4.3. Separation of LP and Subevents Via Waveform Classification

[36] We now apply the classification developed in section 4.2 to the 42,426 events detected at BLIS between 4 and 16 November 2004 (the events analyzed in section 3). As in previous studies [*Stephens and Chouet*, 2001; *Thelen et al.*, 2008; *Matoza et al.*, 2009b], we observe a gradual evolution of the event waveforms as a function of time during this

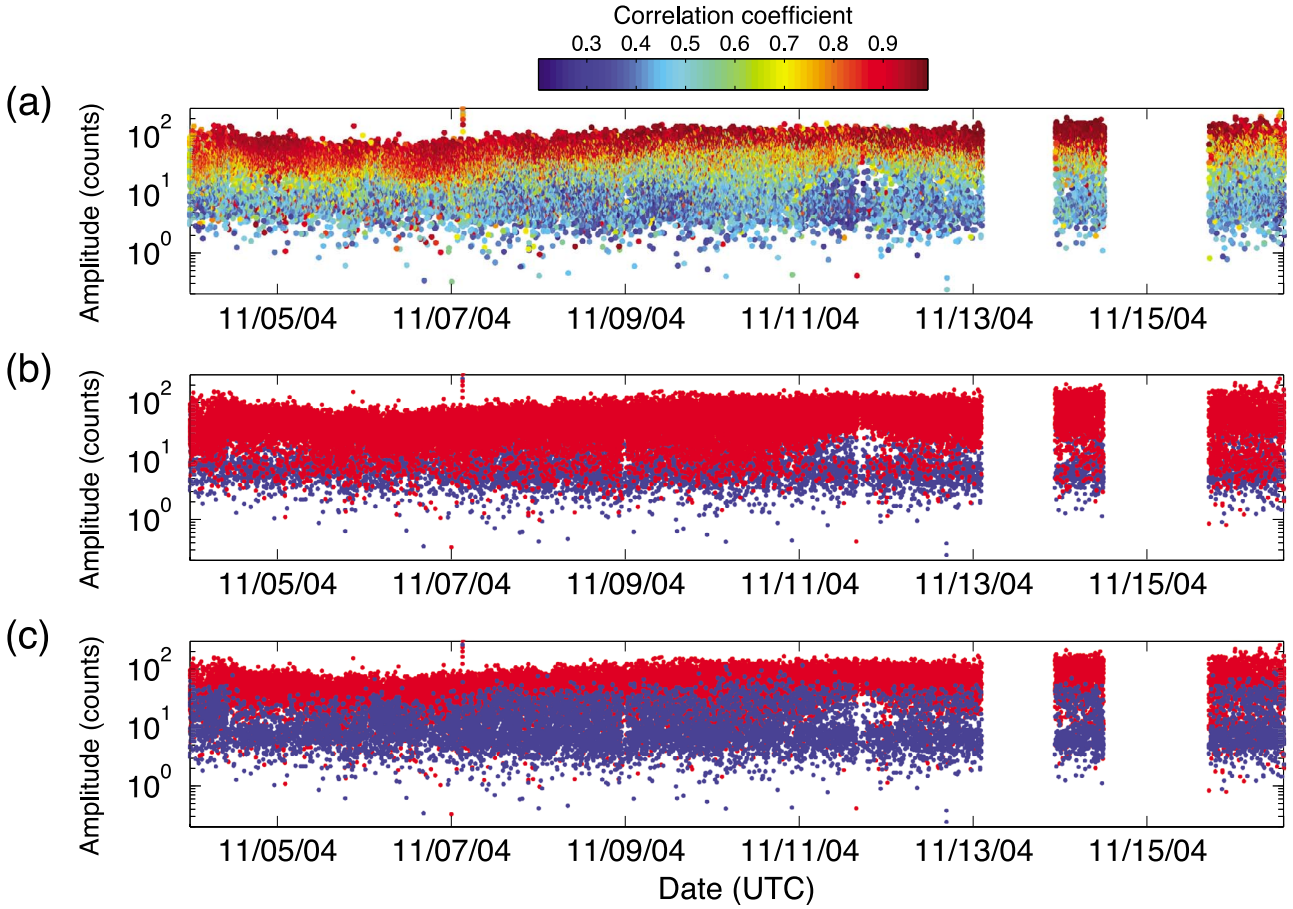

Figure 9. (a) Amplitude of the 42,426 events in the 4–16 November 2004 sequence at BLIS (same data as Figure 4) with events color scaled by the correlation coefficient with a time-evolving master. The time-evolving master is initiated as the master stack waveform of family 1 (section 4.2). (b) Events separated on the basis of cross correlation with time-evolving masters corresponding to family 1 (Figure 9a) and family 2. Red dots correspond to all events correlating with family 1 or 2 with CC > 0.6. Blue dots are all events not correlating with family 1 or 2 with CC > 0.6. (c) Same as Figure 9b, but the blue dots are plotted on top of the red dots to illustrate the overlapping nature of the amplitude distribution of these events. Note that the classification is more successful at separating the overlapping amplitude distributions than the simple amplitude threshold used in Figure 4a.

time period. This "drift" in the master event results in an appreciable change in CC values throughout this time period. To account for this, we follow *Stephens and Chouet* [2001] and utilize a time-evolving master event. The master event is updated every time a new event is detected which has CC > 0.7. The new master event is obtained by stacking two waveforms, where the first waveform represents a normalized version of the current master event scaled by a factor of 0.9, and the second waveform represents a normalized version of the newly detected event scaled by a factor of 0.1. The results of applying this procedure for a master event initially based on family 1 are shown in Figure 9a. Here we replot the scatterplot of Figure 4a with the points color coded according to their CC with the time-evolving master. We note in Figure 9a the presence of relatively small-amplitude events that have high CCs with the dominant waveform family. This demonstrates that waveform correlation is not simply a function of event amplitude.

[37] We assume that the results of section 4.2 (Figure 8) apply to this longer time period and remove families 1 and 2. This defines two groups of seismic events based on waveform alone. Figures 9b and 9c show these two groups of events plotted with different color symbols. We note that since the measured CC is dependent on both the "true" differences in waveform and differences in signal-to-noise ratio caused by differences in individual waveform amplitude, our waveform classification procedure cannot be considered "perfect". For example, some bimodal structure is still evident in the amplitude distribution of the blue dots in Figure 9c.

[38] Figures 10a–10c are histograms of event amplitudes for events in the 4–16 November 2004 sequence at BLIS. Figure 10a shows all of the events, Figure 10b shows just the events belonging to the dominant LP class (i.e., all events extracted with master waveforms from families 1 and 2), while Figure 10c shows events not belonging to the dominant LP class. Similar to Figure 8, Figure 10 illustrates the effectiveness of our waveform classification procedure. We note that the event amplitudes in Figure 10b extend all the way down to the smallest values of amplitude shown on the plot, highlighting the range of amplitudes in the dominant LP

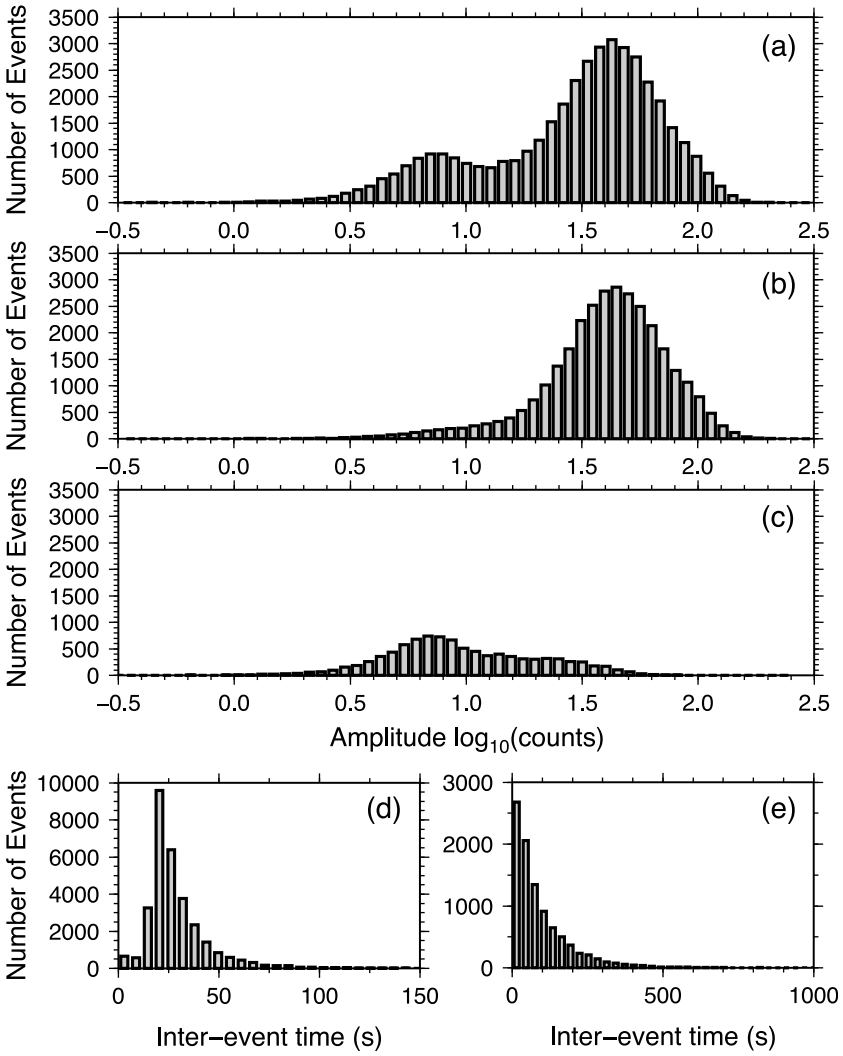

Figure 10. Amplitude and interevent time distribution of events classified according to waveform. (a) Amplitude distribution (log scale, counts) for all events in the 4–16 November 2004 sequence at BLIS (same as Figure 5a). (b) Amplitude distribution of events in Figure 10a belonging to the dominant LP waveform class (i.e., cross correlating with family 1 or 2 with CC > 0.6). (c) Amplitude distribution of all remaining events in Figure 10a not shown in Figure 10b. Note that the events in Figure 10a have a bimodal distribution, whereas events in Figures 10b and 10c have a single mode. Waveform cross correlation provides a means to separate the overlapping amplitude distributions. (d) Interevent time distribution of events shown in Figure 10b. (e) Interevent time distribution of events shown in Figure 10c.

class. The shape of this amplitude distribution indicates that impulsive pressure transients in the LP source region can take place at a large range of event amplitudes, but that an event amplitude of ~40 counts (the mode) is the most likely.

[39] We also note that none of the events fit a classic Gutenberg-Richter (G-R) power law describing ordinary tectonic earthquakes. The G-R power law is given by

$$\log_{10}(N) = a - bM, \tag{3}$$

where N is the number of events with magnitude greater than or equal to M, a and b are constants, and b is the b value. The histogram shown in Figure 10a shows two clearly defined modes corresponding to the dominant LP class and the subevents. The presence of these modes indicates that the G-R power law is not applicable. A similar conclusion was reached for drumbeats at MSH by *Moran et al.* [2008a] and *Horton et al.* [2008]. The G-R power law implies self-similarity or scale invariability of earthquake event sizes, which means that there is no characteristic event size. On the contrary, the presence of the two modes in the histogram of Figure 10a indicates two very prominent characteristic event sizes. Instead, Figure 10a is more similar to the LP swarm sequences accompanying the 1989–1990 eruption of Redoubt [*Lahr et al.*, 1994; *Stephens and Chouet*, 2001]. *Lahr et al.* [1994] found that VT event sequences at Redoubt reasonably fit a classic G-R power law, in harmony with the idea that VT events result from shear fracture and brittle failure. However, *Lahr et al.* [1994] found that LP event sequences did not fit a G-R power law, and instead exhibited a bimodal distribution in magnitude. This conclusion was later confirmed by *Stephens and Chouet* [2001] using a greater

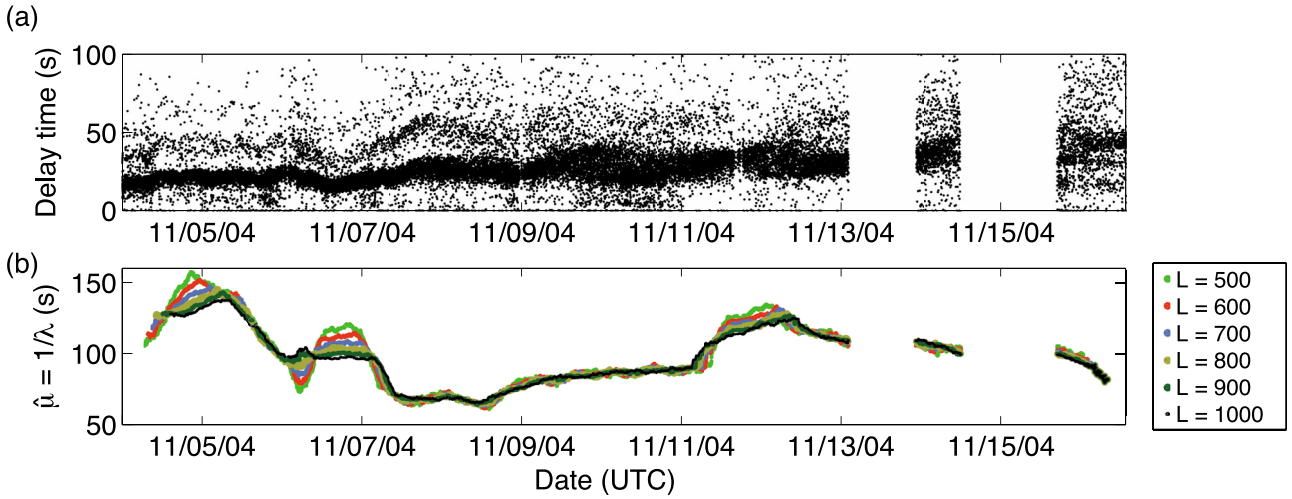

Figure 11. (a) Interevent time (s) of LP waveform class as a function of time for the 4–16 November 2004 sequence at BLIS. These events have a sharply peaked modal interevent time of ~20 s (Figure 10d). This mode changes as a function of time, as seen by the gradual shift of points to higher values of delay time during this time period. Note that there is at least one delay time "harmonic" or integer multiple of the modal delay time. This is a result of occasionally missing events in the initial event picking routine. (b) Poissonian $\hat{\mu} = 1/\lambda$ (s) as a function of time for the subevents during this time period (Figure 10e). The maximum likelihood estimate $\hat{\mu}$ (y axis) is computed at the time of every single event t_{event} in the sequence, on a window of L events centered on t_{event}. The parameter L is varied from 500 to 1000 in this plot as shown in the legend.

number of earthquakes. We have also obtained a bimodal distribution in event amplitude. This therefore appears to be a characteristic common to LP sequences at both MSH and Redoubt. We note that *Stephens and Chouet* [2001] also found that the smaller-amplitude "secondary events" were only observed at the closest seismic stations, and the cross-correlation results of these events are very similar to those described in section 4.2. This suggests that the subevents accompanying LP events at MSH discussed in this study are directly analogous to the small "secondary" events accompanying the LP events at Redoubt [*Stephens and Chouet*, 2001].

[40] The interevent time distribution for the dominant waveform class (Figure 10d) has a sharp peak at ~20 s. This is in harmony with Figure 5b, and ~20 s therefore represents the most common time delay between events in the dominant LP class during the time period analyzed. The subevents (Figure 10e) are well described by an exponential distribution, verifying the results obtained when using our more crude classification scheme (section 3.3). We find that $\mu = \frac{1}{\lambda} \sim$ 90 s provides the optimal fit to the exponential distribution using the KS test procedure outlined in section 3.3.

4.4. Time Dependence of Interevent Times

[41] The analysis so far has neglected nonstationarity or temporal dependence of the event characteristics. Here we briefly investigate time variations in the interevent time for the dominant LP class. We also investigate nonstationarity in the parameter μ describing the exponential interevent time distribution for the subevents. Figure 11a shows the temporal dependence of the interevent times for the dominant LP class (i.e., all events shown in red in Figures 9b and 9c). As seen in Figure 10d, the dominant LP class of events has a sharply defined interevent time distribution peaked at ~20 s. This interevent time changes slightly throughout this time period. We see a gradual increase in the average interevent time from ~17 s on 4 November 2004 to ~42 s on 15 November 2004. There is some complex structure to this change in interevent time, which may relate to complex dynamics in a pressurized hydrothermal system. Such variability was also observed over longer time scales during the 2004–2008 MSH eruption [*Moran et al.*, 2008a]. We note that there is at least one delay time "harmonic", or integer multiple of the modal delay time. This is likely a result of occasionally missing events in the initial event picking routine (see similar artifact discussed by *Ottemoller* [2008]).

[42] For the subevents, we assess changes in the parameter μ of the best fitting exponential distribution as a function of time. Here, we calculate the maximum likelihood estimate for μ, denoted $\hat{\mu}$, simply by

$$\hat{\mu} = \frac{dt_{sum}}{L}, \tag{4}$$

where dt_{sum} is the sum over all the interevent times for the time period (i.e., the time between first and last events in the time window), and L is the number of events defining the time window. We compute $\hat{\mu}(t_{event})$ at the time t_{event} of every event in this sequence using a window of L events surrounding the time t_{event}. The parameter L is varied from 500 to 1000 events in Figure 11b. Low values of L result in less robust estimates $\hat{\mu}$ at any particular time, but allow the assessment of shorter time variations in $\hat{\mu}$. Large values of L result in smoother curves for $\hat{\mu}$ with more reliable estimates. The same general trends are observed in all curves, corresponding to smooth changes in the "average" interevent time μ for subevents. The interevent time for LPs undergoes a sharp bend just before 6 November 2004 (Figure 11a) at the same time that the change

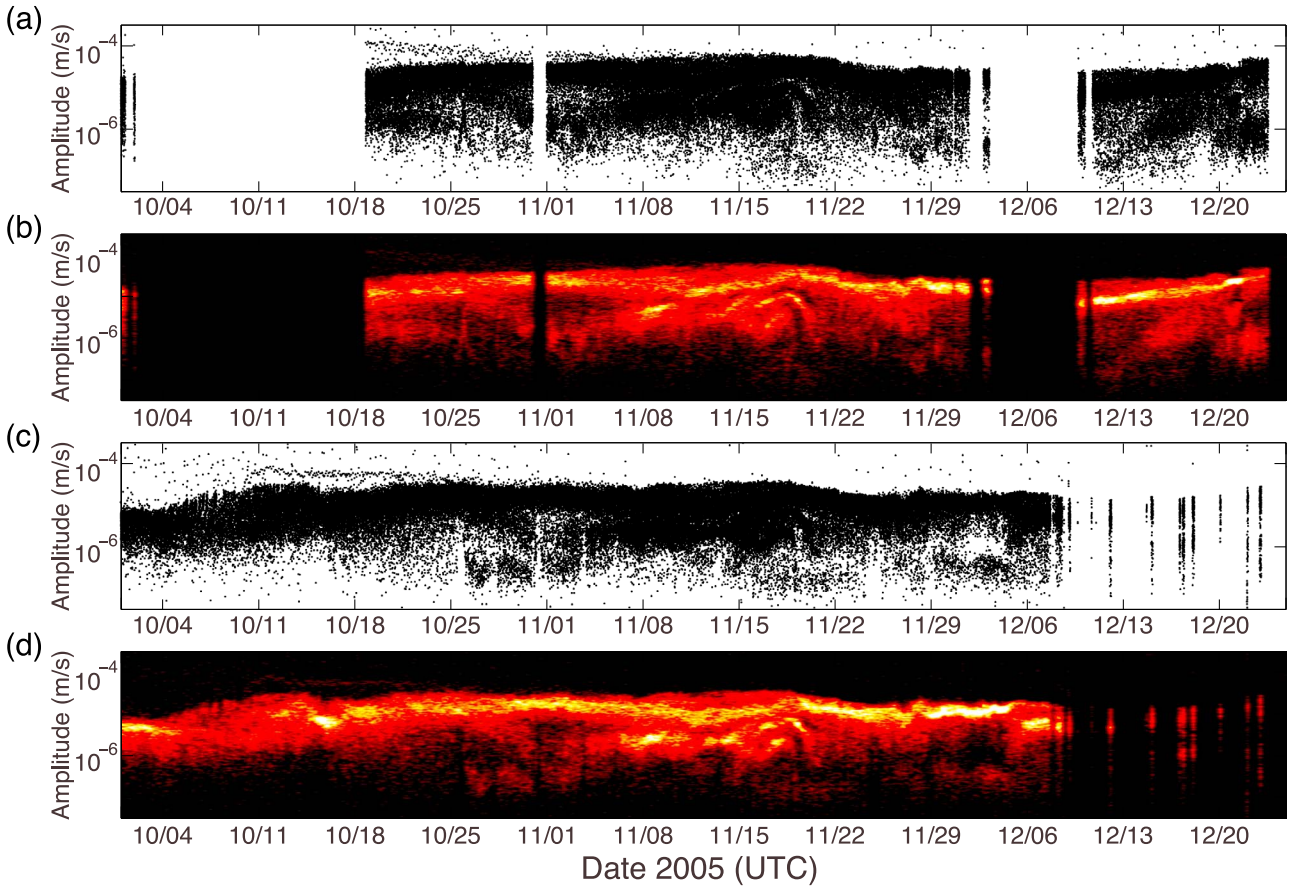

Figure 12. Events triggered at broadband stations S04 and S20 from 1 October to 24 December 2005. (a) Scatterplot of event amplitudes (m/s, log scale) at S04. (b) Shaded image corresponding to density of points shown in Figure 12a. Black-red-orange-white indicates increasing density of points in the scatterplot (Figure 12a). (c and d) Same as Figures 12a and 12b but for station S20. Note the complex temporal dependence of event amplitude. The temporal dependence of the subevents differs from that of the main cluster of events.

in μ for the subevents exhibits a change in slope (Figure 11b), however, little other correlation is found. This indicates that there are no particularly strong correlations between the delay time of the dominant LP events and the average triggering rate of the subevents.

5. Method Applied to Broadband Stations

[43] The analysis developed in sections 3 and 4 for observations at BLIS provides a useful framework for understanding a series of more complex observations at broadband stations S04 and S20 from October to December 2005 (Figure 12). This time period was chosen for analysis as it represents a time during the seismic station deployment of *Waite et al.* [2008] when LP events again began occurring with regular interevent time spacing [*Moran et al.*, 2008a] (see section 3). Figure 12 shows the amplitude of STA/LTA picks of S04 and S20 vertical velocity data between 1 October and 24 December 2005. During this time period, the number of triggered events was 97,455 at S04 (Figures 12a and 12b), and 98,688 at S20 (Figures 12c and 12d). The difference in these numbers is largely due to the difference in data availability (Figure 12). The event amplitude distribution at BLIS discussed in sections 3 and 4 is clearly bimodal (Figure 5a) and approximately stationary during the 2 weeks analyzed (Figures 4 and 11). In contrast, the amplitude distribution for events triggered at S04 and S20 from October to December 2005 exhibits complex temporal evolution, with multimodal structure (more than 2 modes) present during some time periods (Figure 12). In addition, the position of the mode of the subevents is closer to the mode of the LPs at S04 during this time period (Figure 13a), making it more difficult to separate clearly the dominant LP class from the subevents without waveform cross correlation.

[44] Figure 13a shows the amplitude distribution of events at S04 shown in Figure 12 between 18 October and 24 December 2005 (96,700 events). Figure 13b shows the amplitude distribution of the dominant waveform class (i.e., all events in Figure 13a correlating with the most typical waveform with CC > 0.75), while Figure 13c shows all remaining events not belonging to this class. The threshold CC value of 0.75 with the arbitrarily chosen master event was selected here to give the optimal separation of LPs and subevents during this time period using only one master waveform family. The results are very similar to those shown in Figure 10, indicating similar overall trends in event

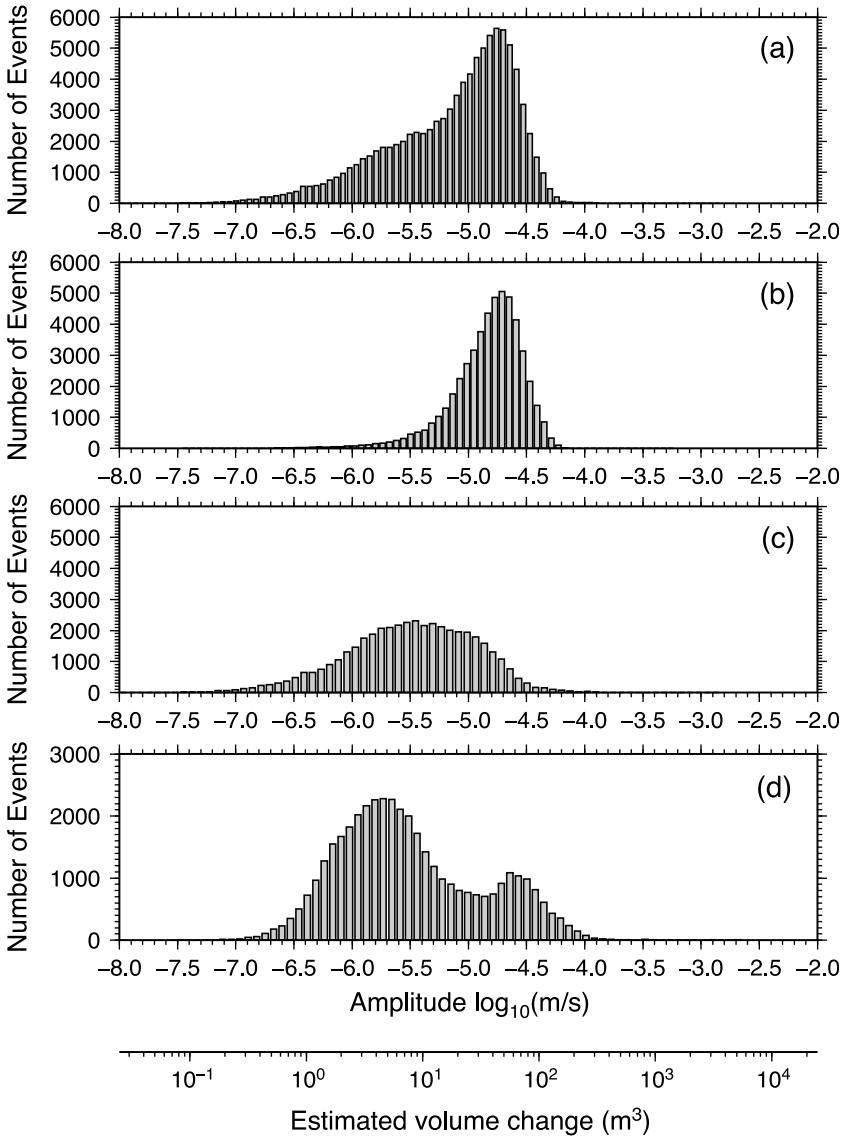

Figure 13. (a–c) Amplitude distribution of events at S04 from 18 October to 24 December 2005 (Figure 12). Figure 13a shows all events triggered at S04 from 18 October to 24 December 2005. Figure 13b shows dominant event family of events shown in Figure 13a. Figure 13c shows all remaining events from Figure 13a not belonging to dominant waveform family (Figure 13b). (d) All events triggered at S04 from 1 to 31 July 2005 (Figure 15). In each case the amplitude is shown in $\log_{10}$ of the vertical velocity waveform in m/s. The amplitudes have been scaled to an estimated volume change (m^3, lower axis) assuming linear scaling of velocity amplitude with source volume change and using the volume change of an event on 2 July 2005 as a reference [*Waite et al.*, 2008].

amplitude despite the more complex temporal dependence seen over this longer time period.

[45] Figure 14 shows the interevent time distributions for the events shown in Figures 13b and 13c. The LP events shown in Figure 13b have a modal interevent time of ~72 s (Figure 14a). This is much longer than the value of ~20 s observed in November 2004 (sections 3.3 and 4.3). Thus, our results confirm the conclusion of *Moran et al.* [2008a] that the overall rate of seismicity slowed between these time periods. The subevents shown in Figure 13c have $\mu \sim 112$ s (Figure 14b), which is also longer than the μ of ~90 s observed in November 2004, although the difference in these numbers is not as drastic. We note that the interevent time distribution shown in Figure 14b consists of a general Poissonian shape superimposed by a small mode at ~72 s. This indicates that our simple procedure of removing only one dominant waveform family has not completely succeeded in removing LP-type events for this complex, temporally evolving data period. The small mode at ~72 s in Figure 14b corresponds to some regularly occurring dominant LP-type events as shown in Figure 14a still being present.

[46] We also consider the time period from 1 to 31 July 2005. Analysis of the amplitude distribution during this time is necessary for the calculation in section 5.1, where we calibrate our observed event amplitudes with the moment tensor inversion results of *Waite et al.* [2008] for an event on

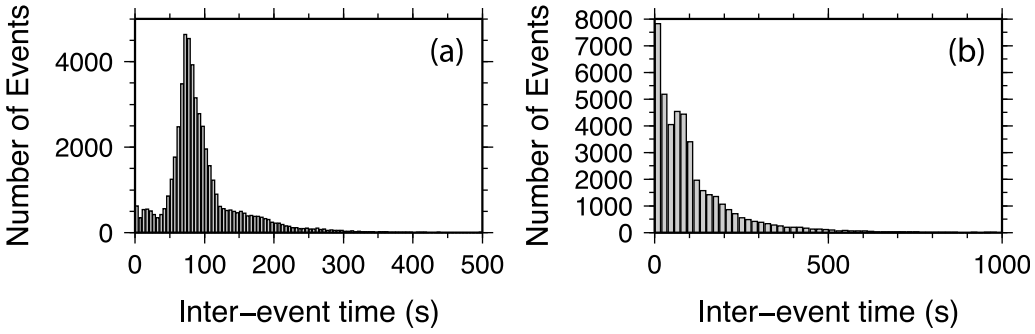

Figure 14. Interevent time distributions of events at S04 from 18 October to 24 December 2005. (a) Interevent time distribution of events shown in Figure 13b. The distribution has a clearly defined mode at ~72 s. (b) Interevent time distribution of events shown in Figure 13c.

2 July 2005. Figure 13d shows the overall event amplitude distribution for 1–31 July 2005. We note that during July 2005 (Figure 13d), the overall event amplitude distribution is different to that observed from 18 October to 24 December 2005 (Figures 13a–13c). Figures 13d and 15 show that the subevents were the dominant (most commonly occurring) class of event during July 2005.

[47] Figure 15a is a scatterplot showing the time dependence of triggered event amplitudes from 1 to 31 July 2005. Figure 15b is the same histogram as that shown in Figure 13d for reference. The temporal evolution of events in Figure 15 exhibits some interesting features. Event amplitudes in Figure 15a occur in two groups, i and ii, where ii have lower amplitude than i and represent subevents. The interevent time of group i (Figure 15c) gradually increases from ~250 s to ~500 s, and then returns back to ~250 s between 3 and 19 July. After 19 July (vertical dashed line, Figures 15a and 15c), the number of events in group i increases (Figure 15a), and the interevent time becomes more scattered (Figure 15c). Such temporal evolution in the seismic triggering process may be related to complex temporal dynamics in a hydrothermal source. Although not shown in Figure 15, the interevent time distribution for the subevents (group ii in Figure 15a) remained Poissonian during this time.

[48] A more complete analysis of the time periods 1–31 July 2005 and 18 October to 24 December 2005 would involve identifying each of the component waveform families during these time intervals. These would likely be strongly time dependent given the observed nonstationarity in event amplitudes (Figure 12). Such a detailed evolving waveform classification procedure is beyond the scope of the present investigation. However, such analysis may enable clear separation of LPs and subevents during these times of complex temporal dependence (e.g., the small mode at ~72 s could be removed from Figure 14b). As stated earlier, a natural focus of future studies would be to track the waveform, spectral, amplitude distribution, and interevent time distribution evolution over the entire 2004–2008 MSH eruption. This could illuminate the connections between the events we report at BLIS during November 2004 (sections 3 and 4) and the series of events recorded on broadband stations during 1–31 July and from 18 October to 24 December 2005 (section 5). Nevertheless, since S04 had a flat response in the frequency band of interest, a more quantitative interpretation of event amplitudes detected at S04 is possible using our existing analysis. This is presented in section 5.1.

5.1. Volume Change and Pressure Drop Associated With MSH Seismicity

[49] *Waite et al.* [2008] provided details of a point source inversion of a particularly large LP event that occurred at 1329:50 UTC on 2 July 2005. By assuming a Poisson solid and dividing the volumetric moment obtained by a shear modulus of 12 GPa, the maximum volume change associated with one cycle of the source time function for this event was calculated at ~770 m^3 in the LP band. Using the value of volume change for this well-characterized event, it is possible to estimate the volume change associated with other similar seismic events at MSH by comparing event amplitudes at a reference station and assuming a linear scaling between vertical velocity waveform amplitude and source volume change.

[50] The maximum amplitude of the vertical velocity waveform at S04 for the 2 July 2005 event is ~3.1×10^{-4} m/s. In Figure 13, this amplitude has been used to scale the observed event amplitude distributions at S04 into an equivalent volume change (lower scale), assuming a linear scaling between vertical velocity waveform amplitude and source volume change. According to this scaling, the dominant LP class during 18 October to 24 December 2005 (Figure 13b) has a modal average volume change of ~45 m^3, while the subevents (Figure 13c) have a modal average volume change of ~9 m^3.

[51] In comparison, Figure 13d shows the event amplitude distribution from 1 to 31 July 2005. This illustrates the overall event amplitude distribution during the time in which the 2 July 2005 event analyzed by *Waite et al.* [2008] occurred. The temporal dependence of event amplitudes during 1–31 July 2005 are shown in Figure 15a. The 2 July 2005 event analyzed by *Waite et al.* [2008] is indicated by a solid red circle and an arrow in Figure 15a, and is significantly larger in amplitude than most other events during this time period. We find that the upper mode (group i, Figure 15a) of LP event amplitudes corresponds to a volume change of ~63 m^3, while the subevents (group ii, Figure 15a) have a volume change of ~5 m^3 during July 2005 (Figure 13d).

[52] We now attempt to relate these volume change estimates to a pressure drop in a fluid-filled crack source. The

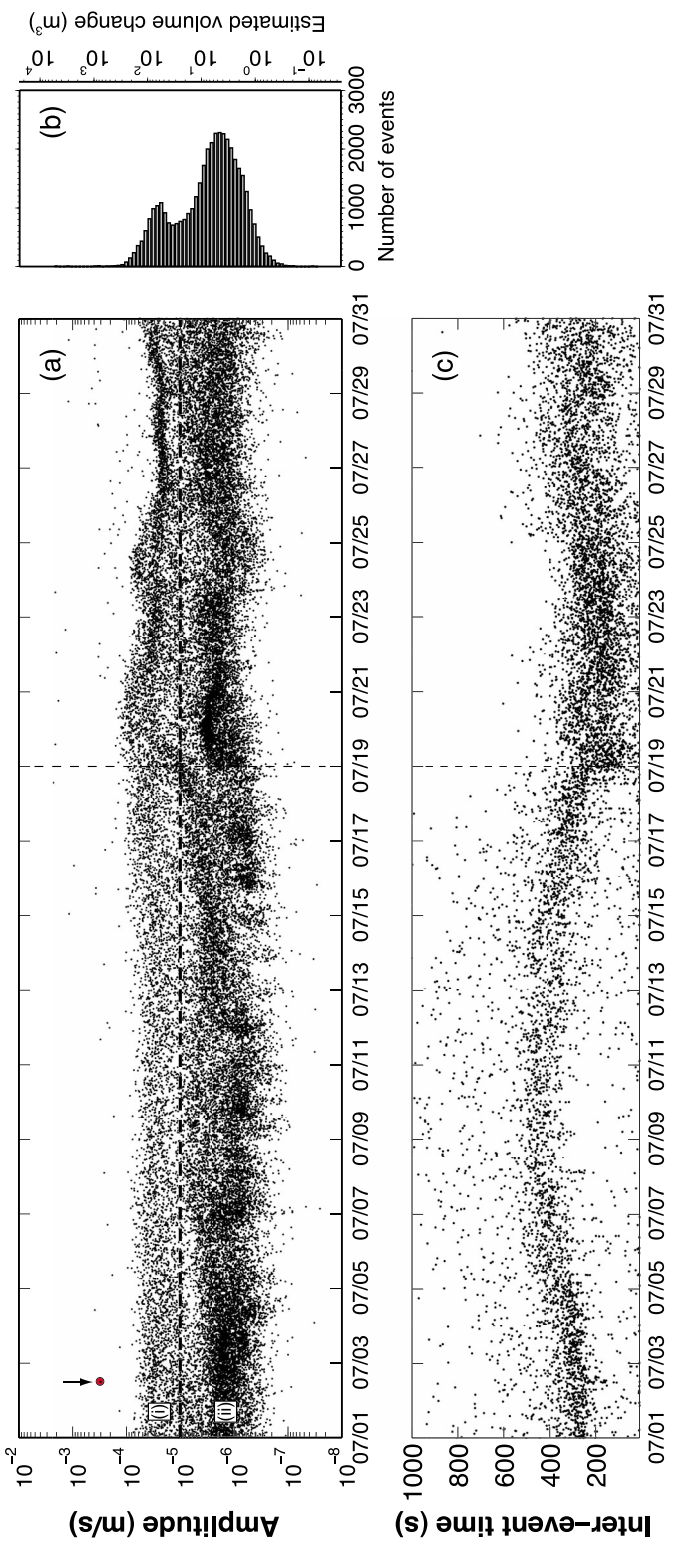

Figure 15. Events triggered at broadband station S04 from 1 to 31 July 2005. (a) Scatterplot of event amplitudes (m/s, log scale) at S04. Solid red circle and arrow indicate the large-amplitude event at 1329:50 UTC on 2 July 2005 analyzed by *Waite et al.* [2008], on which the volume change scale shown in Figures 15b and 13 is based (see text for details). (b) Histogram of all events shown in Figure 15a (same as Figure 13d). Estimated volume change is as shown in Figure 13. (c) Interevent time (s) of events with amplitude $>1 \times 10^{-5}$ m/s (i.e., events i plotting above horizontal dashed line in Figure 15a).

pressure drop in a penny-shaped crack is given by, e.g., *Chouet et al.* [2006]:

$$\Delta P = \frac{3}{4}\frac{\mu(\lambda+\mu)}{\lambda+2\mu}\left(\frac{\Delta V}{a^3}\right), \quad (5)$$

where λ and μ are the Lamé parameters, a is the crack radius, and ΔV is the volume change in the crack. For an order of magnitude estimate, we assume a penny-shaped crack with area πa^2 equivalent to the area of the 100 m × 200 m crack postulated by *Waite et al.* [2008] and obtain a radius $a \sim 80$ m. A crack with area 100 m × 200 m was considered by *Waite et al.* [2008] to be large enough to accommodate the volume change of 770 m^3 obtained for the 2 July 2005 event with a crack aperture opening and closing by ~4 cm (each crack wall having a peak-to-trough displacement of ~2 cm). For instance, for a crack with an equilibrium aperture of 5 cm this would yield a minimum crack aperture of ~3 cm at maximum deflation, and a maximum aperture of 7 cm at maximum inflation. Assuming a Poisson solid with $\lambda = \mu = 12$ GPa, equation (5) yields a pressure drop in the crack of ~9 MPa for the 2 July 2005 event (volume change of 770 m^3) imaged by *Waite et al.* [2008]. The dominant class of LPs during October–December 2005 (Figure 13) correspond to a pressure drop of ~0.5 MPa (volume change of 45 m^3), while the subevents correspond to a pressure drop of ~0.1 MPa (volume change of 9 m^3), assuming the same crack system (i.e., the same effective radius a) for these events. For typical LP events in July 2005, the pressure drop is ~0.7 MPa (volume change of 63 m^3), while the subevents correspond to a pressure drop of ~0.06 MPa (volume change of 5 m^3). The implications of this for the source mechanism of the events are discussed in section 6.

[53] The above pressure change estimates assume the same crack system for the large 2 July 2005 LP event analyzed by *Waite et al.* [2008] and all LP events and subevents. LP event waveforms usually evolved gradually throughout the 2004–2008 eruption of MSH. The assumption of a similar crack system with a similar effective radius a therefore seems reasonable for the majority of LP events. *Waite et al.* [2008] performed waveform inversion on several LP events in July 2005 that had more typical amplitudes than the larger 2 July 2005 event. These inversions revealed essentially the same waveform and source mechanism as the larger 2 July 2005 event. This indicates that the 2 July 2005 event and other larger LP events simply represent a larger pressure drop in essentially the same source mechanism as the typical LPs. By extension, Figures 10 and 13 show that some subevents have the same waveforms as ordinary LP events, indicating that these subevents correspond to the same crack system as the LP events and the large 2 July 2005 LP event. Furthermore, Figure 2b shows that subevents and LP events have a similar frequency content. This suggests that subevents and LP events may be sourced in cracks of comparable size. However, it should be pointed out that even if the subevents are sourced in the same crack system as the 2 July 2005 LP event, subevents may represent pressure transients in small subvolumes of the crack system with smaller effective radii a. In this case, the estimated pressure changes may increase significantly due to the $1/a^3$ term in equation (5). In addition, other subevent families did not correlate with the dominant LP class and may be sourced elsewhere (Figures 10c and 13c). These subevents may be sourced, for example, in smaller cracks within a dendritic network of hydrothermal cracks with smaller effective radii a. In this case, the above pressure drop estimates for subevents would be lower bounds, and the localized pressure changes associated with subevents might be significantly higher.

5.2. LPs During the 8 March 2005 Phreatic Explosion

[54] We find the maximum amplitude of the velocity waveform at STD for the 2 July 2005 event to be ~1.2×10^{-4} m/s. For the LP sequence shown in Figure 3b, ~34 LP events occur during the time in which the broadband infrasound signal is recorded (i.e., the duration of the explosion). Neglecting the subevents, these 34 LP events have a typical amplitude of ~4×10^{-5} m/s at STD throughout this sequence. We note that overall event amplitudes were higher in March 2005 than in July, or October–December 2005 [*Moran et al.*, 2008a]. Assuming a linear scaling between velocity waveform amplitude and source volume change, the minimum volume change for each event is then ~$770 \times (4 \times 10^{-5})/(1.2 \times 10^{-4}) \sim 250$ m^3, and the 34 LP events correspond to a volume change of ~8500 m^3 in a ~35 min time period.

[55] Tephra sampling and ash dispersal reports for the 8 March 2005 explosion suggested an erupted tephra volume of $>10^5$ m^3 (dense rock equivalent) [*Mastin*, 2007]. This estimate does not include the volume of water expelled during the event. In comparison, the LP crack source postulated in section 5.1 has a much smaller volume of ~$200 \times 100 \times 0.05 \sim 10^3$ m^3 (we consider this crack volume as large enough to accommodate the volume change of 770 m^3 obtained for the 2 July 2005 event). Furthermore, the total volume change of ~8500 m^3 implied for LP seismicity during the 8 March 2005 explosion is at least 1 order of magnitude smaller than the estimated tephra volume of $>10^5$ m^3. This large discrepancy in volumes suggests that the LP crack source postulated by *Waite et al.* [2008] would not be a large enough fluid and tephra reservoir to supply the volume of material erupted during the 8 March 2005 explosion. This suggests that the 8 March 2005 explosion tapped a deeper and larger fluid reservoir than that proposed as the LP source. For example, the 8 March 2005 explosion event may have been fed by a deeper aquifer with greater horizontal extent than the shallow hydrothermal crack postulated as the LP source. This interpretation is also consistent with the seismicity observed during this explosive event (section 2.3). A spasmodic component of the eruption tremor consists of a rapid series of LP events that were triggered during the explosion, but that did not cease once the eruption had finished (1–5 Hz filtered seismic waveforms (Figure 3b)). This indicates that the LP source was perturbed, but not destroyed or drained by the explosion. A deeper aquifer feeding the explosion and a shallow aquifer responsible for LP seismicity may have been loosely connected, such that the rapid pressure changes in the deeper reservoir during the explosion could have triggered rapid pressure changes and LP seismicity in the shallow aquifer. However, once the explosion event had finished, the proposed shallow aquifer presumably had enough fluid to continue generating LP seismicity. As discussed in section 2.3, a separate, broadband component of the eruption tremor (clearly visible in CDWR BHZ waveforms filtered 5–15 Hz (Figure 3b)) may be related to pressure perturbations in the deeper reservoir associated with the explosion. Regardless of

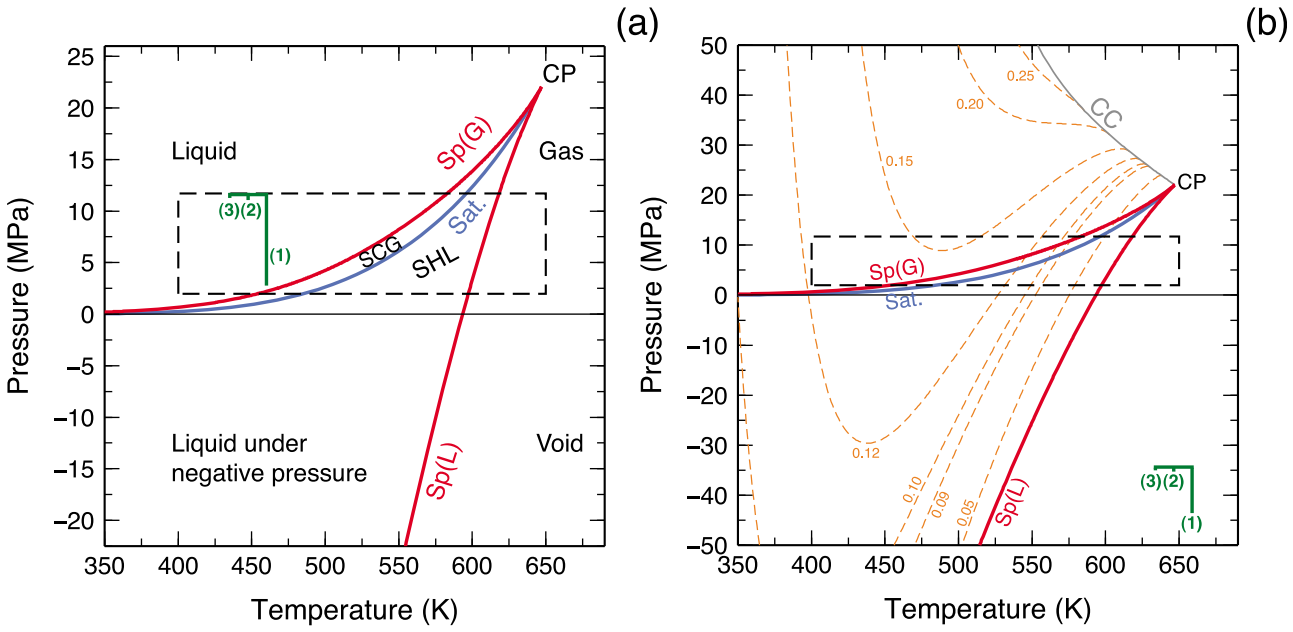

Figure 16. Stable, metastable, and unstable regions of water in *P-T* space according to the IAPWS-95 equations of state [*Wagner and Pruss*, 2002] (following *Thiéry and Mercury* [2009a, 2009b]). In (a) and (b) the blue line is the vapor pressure curve or saturation curve (sat.), while the red lines are the spinodals. Sp(G) is the gas spinodal, and Sp(L) is the liquid spinodal. All three lines meet at the critical point (CP). SCG denotes supercooled gas, while SHL denotes superheated liquid. The dashed black box delineates the assumed range of possible temperature and pressure conditions in the hydrothermal crack source proposed for LPs at MSH (see text for details). Green scale bars correspond to estimated pressure drop (equation (5)) of (1) the 2 July 2005 event (9 MPa), (2) a typical LP event in July 2005 (0.7 MPa), and (3) a typical LP event in October–December 2005 (0.5 MPa) (section 5.1). The pressure drop calculation assumes a penny-shaped crack with radius $a \sim 80$ m in a Poisson solid with $\lambda = \mu = 12$ GPa. The position of the green bars is arbitrary as they are only intended to represent the scales of calculated pressure drop. In Figure 16b the orange dashed lines represent the liquid spinodals for the H_2O-CO_2 binary system (numbers indicate mole fraction of CO_2). The gray line is the H_2O-CO_2 critical curve (CC) [*Thiéry and Mercury*, 2009b].

the geometry of proposed aquifers, the observation that a large volume of fluid was erupted from MSH on 8 March 2005 without stopping LP seismicity suggests that water was in abundant supply at MSH during this event if the seismicity is attributed to a hydrothermal source.

6. Discussion: Explosive Properties of a Hydrothermal System at Mount St. Helens

[56] In sections 2–5, we showed that both LP events and subevents are repetitive events. In general, LP events occur with a fairly regular interevent time spacing, while subevents trigger randomly in time. Both event types were triggered during the 8 March 2005 phreatic explosion event, suggesting a relation between the fluid reservoir feeding this phreatic explosion, and a possible hydrothermal reservoir acting as the LP and subevent source region. Here we discuss the possible thermodynamic changes that may occur in a pressurized hydrothermal crack heated by a magmatic source. We propose that both LP events and subevents could arise from phase changes between liquid water and vapor. More energetic phase changes could result in LP events, while less energetic phase changes involving smaller volumes of fluid could give rise to subevents.

[57] Water can exist in stable solid, liquid, and vapor phases, with these phases coexisting under certain pressure *P*, temperature *T*, and volume *V* conditions [*Collier and Thome*, 1996]. The regions of stability of these various phases in *P-V-T* space are described by the thermodynamic equations of state. In addition, water can be brought into metastable or unstable states [e.g., *Reid*, 1978a, 1978b, 1978c; *Debenedetti*, 1996; *Thiéry and Mercury*, 2009a]. Figure 16a shows the regions of stability and metastability of water in *P-T* space according to the *Wagner and Pruss* [2002] IAPWS-95 equations of state for pure water [after *Thiéry and Mercury*, 2009a]. The saturation curve (blue) in Figure 16a separates the stable regions for liquid and gas phases. Adjacent to the saturation curve are the two metastable regions of water. The superheated liquid (SHL) field represents a metastable liquid that has been brought into *P-T* conditions beyond the stability limits of liquid water, i.e., to a *P* and *T* at which vapor is the stable phase. Conversely, the supercooled gas field (SCG) represents a metastable gas that has been brought into *P-T* conditions at which liquid is the stable phase. Metastable states relax back to stable states via nucleation and phase growth, e.g., cavitation in a superheated liquid. However, rapid temperature or pressure changes may perturb a system beyond a metastable state and into an unstable state. The red

curves are the liquid and gas spinodals (Sp(L) and Sp(G), respectively [*Thiéry and Mercury*, 2009a]). These curves are the theoretical limits for the metastable fields; that is, they are the boundaries between the metastable and unstable regions. For example, a liquid heated at constant pressure from a temperature on the left-hand side of the curve Sp(L) in Figure 16a, toward a temperature on the right-hand side of Sp (L), would undergo a sudden and violent spinodal decomposition back to a more stable biphasic liquid-gas mixture upon intersection of Sp(L) [e.g., *Reid*, 1978a, 1978b, 1978c; *Favvas and Mitropoulos*, 2008; *Thiéry and Mercury*, 2009a]. Spinodal decomposition is a spontaneous and explosive phase separation that occurs throughout the fluid [e.g., *Favvas and Mitropoulos*, 2008; *Thiéry and Mercury*, 2009a]. Phase changes from metastable or unstable states back to more stable states of water in a hydrothermal crack represent a promising source mechanism for both LPs and subevents at MSH.

[58] The generation of LP seismicity within a shallow hydrothermal system as proposed by *Waite et al.* [2008] requires an explanation for the sudden pressure transient or "trigger mechanism" initiating LP resonance. *Waite et al.* [2008] proposed that each LP event corresponds to the sudden rupture of a "valve" sealing the crack. The resultant sudden loss of pressure in the crack causes it to collapse and resonate. *Ohminato* [2006] has also proposed that superheated liquid water in a hydrothermal crack may suddenly vaporize, causing a rapid fluid expansion and causing a valve rupture. These scenarios can be represented by various trajectories in the *P*-*T* space of Figure 16a. The sudden opening of a valve sealing a crack [*Waite et al.*, 2008] can be approximated by an isothermal decompression (i.e., a vertical fall in pressure along a line of constant temperature in Figure 16a). Following the definitions above, liquid decompressions can be classified as either subspinodal or superspinodal. In a subspinodal liquid decompression the pressure drop brings the system only into the metastable region. In a superspinodal liquid decompression the pressure drop brings the system beyond the liquid spinodal, leading to spinodal decomposition. Superspinodal decompressions have been hypothesized as the cause of BLEVEs (Boiling Liquid Expanding Vapor Explosions), a particularly destructive and dangerous type of explosion that can occur in chemical plants or tanks containing pressurized liquids [*Reid*, 1979; *Abbasi and Abbasi*, 2007]. Alternatively, a liquid heated rapidly into the metastable or unstable field [*Ohminato*, 2006] represents some trajectory from left to right in Figure 16a. If this trajectory crosses Sp(L), explosive boiling will result. We note that such rapid heating from left to right in Figure 16a would not necessarily occur along a constant pressure (isobaric) trajectory. As temperature rises, more and more steam bubbles would likely be produced, and both pressure and volume would likely increase as a result. The precise *P*-*T* trajectory may therefore be somewhat complicated.

[59] The dashed black box in Figure 16a represents the range of pressure and temperature conditions that may be present in the hydrothermal crack proposed by *Waite et al.* [2008]. The upper and lower pressure limits assume lithostatic pressure ($P = \rho g z$, where ρ is the density of the overburden, $g = 9.81$ m/s^2 is the acceleration due to gravity, and z is the depth of the crack). The estimates correspond to upper and lower bounds on the assumed density of overburden and depth of the crack (ρ_{hi} = 2650 kg/m^3, ρ_{lo} = 2000 kg/m^3, assumed upper and lower limits on density; z_{hi} = 450 m, z_{lo} = 100 m, assumed upper and lower limits on depth; hence P_{hi} = 11.7 MPa, P_{lo} = 1.96 MPa, upper and lower limits on pressure). We note that growth and collapse of lava spines during the 2004–2008 MSH eruption would lead to a shifting overburden pressure on the proposed LP source with time, which may lead to some of the observed complex temporal dynamics (e.g., Figure 12). The temperature limits are provided simply for discussion, but seem reasonable for water heated by magma which may have temperature ~1500 K. Vertical green bars in Figure 16 represent the magnitudes of pressure drop estimated in section 5.1 for (1) the 2 July 2005 event analyzed by *Waite et al.* [2008], (2) the average LP event in July 2005, and (3) the average LP event in October–December 2005. From initial temperature and pressure conditions close to boiling (i.e., in the region immediately above and to the left of the blue saturation curve in Figure 16a, 500 K $\lesssim T \lesssim$ 575 K, 2.5 MPa $\lesssim P \lesssim$ 10 MPa), the pressure drops 2 and 3 would not be large enough to cause a superspinodal decompression. Here the pressure drops 2 and 3 bring the liquid at most into a metastable state. The pressure change 1 corresponding to the 2 July 2005 event would be a more significant pressure change on Figure 16a. This pressure change corresponds to, for example, a drop from an initial pressure of ~9.1 MPa in the dashed box in Figure 16a back to an atmospheric pressure of ~0.1 MPa. For lower values of starting pressure (e.g., 2.5–7.5 MPa), the pressure change 1 could bring the system into the region of negative pressure. However, the pressure change from this event is not representative of the majority of LP events at MSH during 2004–2008. Occasional, larger pressure drops in the system offer an explanation for larger $M_d > 2$ events observed sporadically throughout the 2004–2008 eruption of MSH [*Moran et al.*, 2008b].

[60] However, the above considerations are for a pure H_2O system. The explosive potential of the system increases significantly by the addition of even a small mole fraction of dissolved volatiles, e.g., CO_2 [*Thiéry and Mercury*, 2009b]. Figure 16b shows the same pure H_2O curves in *P*-*T* space as Figure 16a. However, the liquid spinodals for the binary H_2O-CO_2 system with different values of CO_2 mole fraction are also shown as orange dashed curves [*Thiéry and Mercury*, 2009b]. Note that as the mole fraction of CO_2 increases from 0.05 to 0.12, the position of the liquid spinodal (orange dashed curves) shifts to lower and lower temperatures for the pressure and temperature conditions within our assumed range (i.e., within the dashed black box in Figure 16b). In particular, for temperatures between ~500 and ~600 K, and pressures of ~0–10 MPa, CO_2 mole fractions of ~0.05–0.12 lead to a very unstable system. In this region, as the H_2O-CO_2 liquid spinodals move closer to the saturation curve with increasing CO_2 mole fraction, the pressure drop required to intersect the liquid spinodal from an initial *P*-*T* point on the saturation curve is increasingly reduced. Therefore, as more CO_2 is added to the system, smaller pressure drops can lead to violent superspinodal phase changes, and the seismogenic potential of the system (i.e., the potential of the system to generate seismic energy) is increased.

[61] For instance, suppose that *P*-*T* conditions in a hydrothermal crack are close to the saturation curve on Figure 16b, with $P \sim 5$ MPa and $T \sim 550$ K, and both *P* and

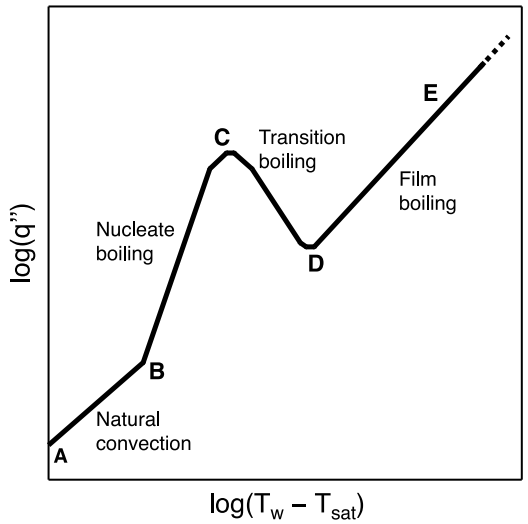

Figure 17. Schematic of the pool boiling curve [after *Collier and Thome*, 1996; *Tong and Tang*, 1997; *Hewitt*, 1998]. This is a log-log relationship between heat flux q'' and wall superheat $T_w - T_{sat}$. A–B, natural convection; B–C, nucleate boiling; C–D, transition boiling; D–E, film boiling.

T are gradually increasing as a result of magmatic heating. Now suppose that the pressure suddenly reaches the critical pressure threshold for opening a "valve" sealing the crack. The valve suddenly opens, and pressure in the crack drops rapidly from ~5 MPa by an amount ~0.5 MPa corresponding to a typical LP event in October–December 2005. This pressure change sends the H_2O-CO_2 system into the metastable region, whereupon vapor bubbles will suddenly expand, leading to a rapid pressure buildup in the crack. This increasing pressure may then induce the collapse and cavitation of the bubbles and may generate a shock wave which could reverberate in the crack. The large pressure pulse associated with the shock wave can then result in crossing the liquid spinodal, causing more catastrophic failure and rapid fluid ejection through the valve sealing the container. This mechanism is known as a BLCBE (Boiling Liquid Compressed Bubble Explosion) and is thought to be responsible for some observed complexities in industrial BLEVE explosions [*Abbasi and Abbasi*, 2007]. The details of this process seem consistent with observations at MSH. For instance, the initial pressure drop associated with valve opening is consistent with the dilatational first motions observed in LP seismic waveforms, while the rapid venting of fluid from a container is consistent with production of infrasonic signals in the atmosphere [*Matoza et al.*, 2009b]. In the case of the 2 July 2005 event, the pressure drop from a starting point of ~5 MPa would be enough to immediately cause a superspinodal decompression in a H_2O-CO_2 system.

[62] Subevents could arise from such a system in a variety of ways. Whereas the regular interevent times of the LP events point to a recharge process, the random temporal occurrence of the subevents is more consistent with random pressure and phase changes dispersed throughout a hydrothermal system. The idea of randomly occurring phase changes in a distributed crack system involving small volumes of ~5 m^3 (section 5.1) is consistent with the conclusion from section 4.4 that subevents arise from a random background process accompanying the cyclic LP event source process. The repetitive nature of many of the subevent waveforms (section 4.2) is also indicative of a repetitive, nondestructive source process. One explanation is that random void collapse events may occur at preferential nucleation sites within a hydrothermal system, resulting in repetitive waveforms. Some subevents have waveforms belonging to the main LP waveform family (Figures 10 and 13). This indicates that the same or a very similar fluid source process is responsible for these subevents and LPs.

[63] The repetitive interevent time of ~20 s for LP events in November 2004 is indicative of a rapidly rechargeable cyclic failure process. This indicates that the proposed "valve" on the crack should reseal, and pressure conditions in the crack should recharge to the conditions for valve failure within ~20 s in November 2004, or ~72 s in October–December 2005. Such a process requires an abundant hydrothermal fluid supply, and a rapid rate of heating. The LP point source location of *Waite et al.* [2008] was directly below the active 2004–2008 lava dome. The LP point source location is also ~400 m to the southeast and ~250 m shallower than the point source location of very long period (VLP, 8–40 s) events [*Waite et al.*, 2008]. The VLP events were attributed to inertial forces in a magma conduit. The location of the VLP events therefore gives an indication of the location of the magma conduit. For the LP crack extent of 100 m × 200 m considered by *Waite et al.* [2008] and given the spatial reach of the magma conduit and extruding spine, and further accounting for point source location uncertainties, it seems reasonable to assume that the hydrothermal system and magmatic system were essentially in close contact. We do not consider the mechanism of heat transfer from the magmatic to hydrothermal system quantitatively. The heat transfer may arise, for instance, from a flux of hot volatiles exsolving from the magma conduit and entering the hydrothermal system. In this case, the volatiles may play a critical role both in supplying heat, and in controlling the position of the liquid spinodal curve (Figure 16b). In another scenario, heat transfer may result from direct contact of hydrothermal water with magma. This may correspond to a boiling heat transfer process, which can be a very efficient mechanism of heat transfer [*Tong and Tang*, 1997; *Hewitt*, 1998].

[64] A hydrothermal system heated by direct contact with magma might be analogous to a *pool boiling* process, which is a situation where boiling takes place on a heated surface submerged in a pool of initially nonmoving liquid (that is, there is no mechanically induced circulation of the liquid as is found in man-made settings) [*Tong and Tang*, 1997]. We describe briefly some characteristics of pool boiling, as they offer insight into possible mechanisms of subevent generation. Figure 17 is a schematic of a pool boiling curve [after *Tong and Tang*, 1997; *Hewitt*, 1998], which is a log-log plot of the heat flux q'' versus the wall superheat $T_w - T_{sat}$, where T_w is the temperature of a heating surface and T_{sat} is the saturation temperature of the liquid (see blue curve in Figure 16). At low values of wall superheat (branch A–B in Figure 17), heat transfer takes place via natural convection. As $T_w - T_{sat}$ increases, the liquid becomes superheated near the wall and bubbles begin to form. This corresponds to the nucleate boiling regime (B–C in Figure 17). Eventually, the number of bubbles becomes very high and an insulating blanket of vapor forms on the heating surface. The peak in the

boiling curve marks the upper limit of nucleate boiling where liquid access to the heating surface is restricted by blankets of steam on the surface. The transition boiling regime (C–D in Figure 17) is marked by the formation of an unstable vapor blanket over the heating surface and intermittent wetting of the surface associated with the release of large patches of steam. This regime is characterized by a decline in heat flux with increasing wall superheat and it ends when the heating surface is blanketed by a continuous film of steam (the minimum D in Figure 17, called the Leidenfrost point). A regime of stable film boiling occurs beyond the Leidenfrost point (regime D–E in Figure 17), marked by increasing heat flux with increasing wall superheat. Heat transfer is controlled by radiation in the regime D–E. The shape and position of the pool boiling curve is affected in a complicated way by parameters such as the pressure, the material constituting the heating surface, the roughness and geometry of the heating surface, and the presence of dissolved impurities in the water. This makes it difficult to perform a quantitative analysis of the heat transfer process from magma to water at this stage.

[65] Nevertheless, subevents could arise from such a pool boiling process via random pressure disturbances at the heating surface. For instance, in the transition boiling regime C–D of Figure 17, the intermittent collapse of a steam film blanketing the heating surface can force contact of magma and water, resulting in significant thermohydraulic explosions [e.g., *Wohletz*, 1986; *Zimanowski et al.*, 1991]. Thus, magma-water interactions offer many plausible scenarios for the generation of subevents at MSH.

7. Conclusions

[66] During 2004–2005, a repetitive series of LP seismic events at MSH were accompanied by a continuous triggering of subevents. In contrast to the LP events, which generally occurred with a regular interevent time spacing, the subevents occurred randomly in time. The amplitude distributions of LPs and subevents exhibited complex temporal dependence over week- to month-long durations. Waveform cross correlation indicates that the majority of LP events and subevents resulted from rapidly rechargeable, nondestructive source processes. However, the waveforms for the LP events are generally different from those of the subevents. This indicates that the subevents result from a separate, random, but repetitive process, perhaps only loosely coupled to the main LP source process. The observed characteristics of the subevents seem consistent with a fluid source process. However, the subevents may also be attributed to a shear faulting process.

[67] The regular interevent time of the main LP event sequence suggests a recharge failure process with a modal recharge time of ~20 s in November 2004. We suggest that this recharge process may consist of the rapid heating of water and dissolved volatiles in a hydrothermal crack. Heat transfer into the hydrothermal system may take place via contact with magma (boiling heat transfer), or by hot volatiles escaping the magma and entering the hydrothermal system. In either case, heating of water in a hydrothermal crack may cause pressure to rise to a threshold pressure for rupture of a "valve" sealing the crack. If the pressure and temperature conditions in the hydrothermal crack are close to the saturation curve when the valve opening occurs, the pressure drop resulting from the valve opening may cause a chain of complex and possibly violent phase changes. Such phase changes between liquid and vapor represent promising candidates for triggering LP events and subevents. The addition of a small mole fraction of CO_2 into the hydrothermal water could significantly lower the pressure drops required for a superspinodal decompression, and thereby increase the seismogenic potential of the system.

[68] Finally, we observed that both LP events and subevents were triggered rapidly during the 8 March 2005 phreatic explosion, and did not cease afterward. This triggering in relation to the rapid ejection of steam from the subsurface system suggests that both seismic event types originated from a region of the subsurface hydrothermal system that was perturbed, but not destroyed or drained by the 8 March 2005 explosion. The volume of tephra and fluid erupted during the 8 March 2005 event also suggests that the explosion was fed by a deeper and more extensive hydrothermal system than that proposed for the LP and subevent source. Larger-amplitude events, such as the 2 July 2005 event analyzed by *Waite et al.* [2008], represent significant pressure perturbations in a subsurface hydrothermal crack that could perturb the hydrothermal system into an unstable state. The fact that such events did not lead to routine phreatic explosions further suggests that the LP seismic source region beneath MSH represented a smaller and shallower volume than the reservoir feeding the 8 March 2005 phreatic explosion.

[69] **Acknowledgments.** We thank the staff of the Cascades Volcano Observatory for many useful discussions, W. Wagner for providing the IAPWS-95 formulation software [*Wagner and Pruss*, 2002], and R. Thiéry for providing the spinodal curves. Data from BLIS, YEL, and STD were collected by the Cascades Volcano Observatory, while data from S04 and S20 were collected by G. P. Waite. Both were downloaded via IRIS. Data from CDWR were collected as part of the Acoustic Surveillance for Hazardous Eruptions experiment [*Garces et al.*, 2008]. We thank S. C. Moran, S. G. Prejean, two anonymous reviewers, and an Associate Editor for clear and thorough reviews. This work was partially supported by NSF grant EAR-0609669 (PI: M. A. Garcés).

References

Abbasi, T., and S. A. Abbasi (2007), The boiling liquid expanding vapour explosion (BLEVE): Mechanism, consequence assessment, management, *J. Hazard. Mater.*, *141*, 489–519.

Bedrosian, P. A., M. J. Unsworth, and M. J. S. Johnston (2007), Hydrothermal circulation at Mount St. Helens determined by self-potential measurements, *J. Volcanol. Geotherm. Res.*, *160*, 137–146.

Bedrosian, P. A., M. Burgess, and A. Hotovec (2008), Groundwater hydrology within the crater of Mount St. Helens from geophysical constraints, *Eos Trans. AGU*, *89*(53), Fall Meet. Suppl., Abstract V43E-2191.

Bergfeld, D., W. C. Evans, K. A. McGee, and K. R. Spicer (2008), Pre- and post-eruptive investigations of gas and water samples from Mount St. Helens, Washington, 2002 to 2005, in *A Volcano Rekindled: The Renewed Eruption of Mount St. Helens, 2004–2006*, edited by D. R. Sherrod, W. E. Scott, and P. H. Stauffer, *Prof. Paper 1750*, chap. 25, pp. 523–542, U.S. Geol. Surv., Reston, Va.

Caplan-Auerbach, J., and T. Petersen (2005), Repeating coupled earthquakes at Shishaldin Volcano, Alaska, *J. Volcanol. Geotherm. Res.*, *145*, 151–172.

Cashman, K. V., C. R. Thornber, and J. S. Pallister (2008), From dome to dust: Shallow crystallization and fragmentation of conduit magma during the 2004–2006 dome extrusion at Mount St. Helens, Washington, in *A Volcano Rekindled: The Renewed Eruption of Mount St. Helens, 2004–2006*, edited by D. R. Sherrod, W. E. Scott, and P. H. Stauffer, *Prof. Paper 1750*, chap. 19, pp. 387–413, U.S. Geol. Surv., Reston, Va.

Chouet, B. (1985), Excitation of a buried magmatic pipe: A seismic source model for volcanic tremor, *J. Geophys. Res.*, *90*, 1881–1893.

Chouet, B. A. (1996a), Long-period volcano seismicity: Its source and use in eruption forecasting, *Nature*, *380*, 309–316.

Chouet, B. A. (1996b), New methods and future trends in seismological volcano monitoring, in *Monitoring and Mitigation of Volcano Hazards*, edited by R. Scarpa and R. Tilling, pp. 23–97, Springer, New York.

Chouet, B. A., R. A. Page, C. D. Stephens, J. C. Lahr, and J. A. Powers (1994), Precursory swarms of long-period events at Redoubt Volcano (1989–1990), Alaska: Their origin and use as a forecasting tool, *J. Volcanol. Geotherm. Res.*, *62*, 95–135.

Chouet, B., P. Dawson, and M. Nakano (2006), Dynamics of diffusive bubble growth and pressure recovery in a bubbly rhyolitic melt embedded in an elastic solid, *J. Geophys. Res.*, *111*, B07310, doi:10.1029/2005JB004174.

Collier, J. G., and J. R. Thome (1996), *Convective Boiling and Condensation*, *Oxford Eng. Sci. Ser.*, vol. 38, 3rd ed., Clarendon, Oxford, U. K.

Debenedetti, P. G. (1996), *Metastable Liquids: Concepts and Principles*, Princeton Univ. Press, Princeton, N. J.

Dzurisin, D., J. Vallance, T. Gerlach, S. Moran, and S. Malone (2005), Mount St. Helens reawakens, *Eos Trans. AGU*, *86*(3), 25, 29.

Favvas, E. P., and A. C. Mitropoulos (2008), What is spinodal decomposition?, *J. Eng. Sci. Technol. Rev.*, *1*, 25–27.

Fehler, M. (1983), Observations of volcanic tremor at Mount St. Helens Volcano, *J. Geophys. Res.*, *88*, 3476–3484.

Fehler, M., and B. Chouet (1982), Operation of a digital seismic network on Mount St. Helens volcano and observations of long period seismic events that originate under the volcano, *Geophys. Res. Lett.*, *9*, 1017–1020.

Garces, M., D. Fee, D. McCormack, R. Servranckx, H. Bass, C. Hetzer, M. Hedlin, R. Matoza, and H. Yepes (2008), Prototype ASHE volcano monitoring system captures the acoustic fingerprint of stratospheric ash injection, *Eos Trans. AGU*, *89*(40), 377–379.

Gil Cruz, F., and B. A. Chouet (1997), Long-period events, the most characteristic seismicity accompanying the emplacement and extrusion of a lava dome in Galeras Volcano, Colombia, in 1991, *J. Volcanol. Geotherm. Res.*, *77*, 121–158.

Goldstein, P., and B. Chouet (1994), Array measurements and modeling of sources of shallow volcanic tremor at Kilauea Volcano, Hawaii, *J. Geophys. Res.*, *99*, 2637–2652.

Green, D. N., and J. Neuberg (2006), Waveform classification of volcanic low-frequency earthquake swarms and its implication at Soufriere Hills Volcano, Montserrat, *J. Volcanol. Geotherm. Res.*, *153*, 51–63.

Harrington, R. M., and E. E. Brodsky (2007), Volcanic hybrid earthquakes that are brittle-failure events, *Geophys. Res. Lett.*, *34*, L06308, doi:10.1029/2006GL028714.

Hewitt, G. F. (1998), *Handbook of Heat Transfer*, 3rd ed., edited by W. M. Rohsenow, J. P. Hartnett, and Y. I. Cho, chap. 15, McGraw-Hill, New York.

Horton, S., R. D. Norris, and S. Moran (2008), Broadband characteristics of earthquakes recorded during a dome-building eruption at Mount St. Helens, Washington, between October 2004 and May 2005, in *A Volcano Rekindled: The Renewed Eruption of Mount St. Helens, 2004–2006*, edited by D. R. Sherrod, W. E. Scott, and P. H. Stauffer, *Prof. Paper 1750*, chap. 5, pp. 97–110, U.S. Geol. Surv., Reston, Va.

Iverson, R. M., et al. (2006), Dynamics of seismogenic volcanic extrusion at Mount St. Helens in 2004–05, *Nature*, *444*, 439–443.

Kieffer, S. (1981), Blast dynamics at Mount St. Helens on 18 May 1980, *Nature*, *291*, 568–570.

Kumagai, H., and B. A. Chouet (2000), Acoustic properties of a crack containing magmatic or hydrothermal fluids, *J. Geophys. Res.*, *105*, 25,493–25,512.

Kumagai, H., B. A. Chouet, and P. B. Dawson (2005), Source process of a long-period event at Kilauea volcano, Hawaii, *Geophys. J. Int.*, *161*, 243–254.

Lahr, J. C., B. A. Chouet, C. D. Stephens, J. A. Power, and R. A. Page (1994), Earthquake classification, location, and error analysis in a volcanic environment: Implications for the magmatic system of the 1989–1990 eruptions of Redoubt Volcano, Alaska, *J. Volcanol. Geotherm. Res.*, *62*, 137–151.

LaHusen, R. G., K. J. Swinford, M. Logan, and M. Lisowski (2008), Instrumentation in remote and dangerous settings: Examples using data from GPS "spider" deployments during the 2004–2005 eruption of Mount St. Helens, Washington, in *A Volcano Rekindled: The Renewed Eruption of Mount St. Helens, 2004–2006*, edited by D. R. Sherrod, W. E. Scott, and P. H. Stauffer, *Prof. Paper 1750*, chap. 16, pp. 335–345, U.S. Geol. Surv., Reston, Va.

Latter, J. H. (1979), Volcanological observations at Tongariro National Park: 2. Types and classification of volcanic earthquakes, 1976–1978, *Rep. 150*, 60 pp., N. Z. Dep. of Sci. and Ind. Res., Geophys. Div., Wellington.

Malone, S. D. (1983), Volcanic earthquakes: Examples from Mount St. Helens, in *Earthquakes: Observations, Theory and Interpretation*, pp. 436–455, Soc. Ital. Fis., Bologna, Italy.

Massey, F. J. (1951), The Kolmogorov-Smirnov test for goodness of fit, *J. Am. Stat. Assoc.*, *46*, 68–78.

Mastin, L. G. (2007), A user-friendly one-dimensional model for wet volcanic plumes, *Geochem. Geophys. Geosyst.*, *8*, Q03014, doi:10.1029/2006GC001455.

Matoza, R. S., M. A. H. Hedlin, and M. A. Garces (2007), An infrasound array study of Mount St. Helens, *J. Volcanol. Geotherm. Res.*, *160*, 249–262.

Matoza, R. S., D. Fee, M. A. Garces, J. M. Seiner, P. A. Ramon, and M. A. H. Hedlin (2009a), Infrasonic jet noise from volcanic eruptions, *Geophys. Res. Lett.*, *36*, L08303, doi:10.1029/2008GL036486.

Matoza, R. S., M. A. Garces, B. A. Chouet, L. D'Auria, M. A. H. Hedlin, C. De Groot-Hedlin, and G. P. Waite (2009b), The source of infrasound associated with long-period events at Mount St. Helens, *J. Geophys. Res.*, *114*, B04305, doi:10.1029/2008JB006128.

McChesney, P. J., M. R. Couchman, S. C. Moran, A. B. Lockhart, K. J. Swinford, and R. G. L. Husen (2008), Seismic monitoring changes and the remote deployment of seismic stations (Seismic Spider) at Mount St. Helens, in *A Volcano Rekindled: The Renewed Eruption of Mount St. Helens, 2004–2006*, edited by D. R. Sherrod, W. E. Scott, and P. H. Stauffer, *Prof. Paper 1750*, chap. 7, pp. 129–140, U.S. Geol. Surv., Reston, Va.

McNutt, S. R. (1992), Volcanic tremor, in *Encyclopedia of Earth System Science*, vol. 4, edited by L. Brekhovskikh et al., pp. 417–425, Academic, San Diego, Calif.

Moran, S. C., S. D. Malone, A. I. Qamar, W. Thelen, A. K. Wright, and J. Caplan-Auerback (2008a), 2004–2005 seismicity associated with the renewed dome-building eruption of Mount St. Helens, in *A Volcano Rekindled: The Renewed Eruption of Mount St. Helens, 2004–2006*, edited by D. R. Sherrod, W. E. Scott, and P. H. Stauffer, *Prof. Paper 1750*, chap. 2, pp. 27–60, U.S. Geol. Surv., Reston, Va.

Moran, S. C., P. J. McChesney, and A. B. Lockhart (2008b), Seismicity and infrasound associated with explosions at Mount St. Helens, 2004–2005, in *A Volcano Rekindled: The Renewed Eruption of Mount St. Helens, 2004–2006*, edited by D. R. Sherrod, W. E. Scott, and P. H. Stauffer, *Prof. Paper 1750*, chap. 6, pp. 111–127, U.S. Geol. Surv., Reston, Va.

Nakano, M., H. Kumagai, M. Kumazawa, K. Yamaoka, and B. Chouet (1998), The excitation and characteristic frequency of the long-period volcanic event: An approach based on an inhomogeneous autoregressive model of a linear dynamic system, *J. Geophys. Res.*, *103*, 10,031–10,046.

Ohminato, T. (2006), Characteristics and source modeling of broadband seismic signals associated with the hydrothermal system at Satsuma-Iwojima volcano, Japan, *J. Volcanol. Geotherm. Res.*, *158*, 467–490.

Ottemoller, L. (2008), Seismic hybrid swarm precursory to a major lava dome collapse: 9–12 July 2003, Soufriere Hills Volcano, Montserrat, *J. Volcanol. Geotherm. Res.*, *177*, 903–910.

Pallister, J. S., C. R. Thornber, K. V. Cashman, M. A. Clynne, H. A. Lowers, C. W. Mandeville, I. K. Brownfield, and G. P. Meeker (2008a), Petrology of the 2004–2006 Mount St. Helens lava dome: Implications for magmatic plumbing and eruption triggering, in *A Volcano Rekindled: The Renewed Eruption of Mount St. Helens, 2004–2006*, edited by D. R. Sherrod, W. E. Scott, and P. H. Stauffer, *Prof. Paper 1750*, chap. 30, pp. 647–702, U.S. Geol. Surv., Reston, Va.

Pallister, J. S., K. V. Cashman, and J. T. Hagstrum (2008b), Conduit-margin faulting at Mount St. Helens: A seismogenic process?, *Eos Trans. AGU*, *89*(53), Fall Meet. Suppl., Abstract V43E-2186.

Petersen, T. (2007), Swarms of repeating long-period earthquakes at Shishaldin Volcano, Alaska, *J. Volcanol. Geotherm. Res.*, *166*, 177–192.

Ramos, E. G., M. W. Hamburger, G. L. Pavlis, and E. P. Laguerta (1999), The low-frequency earthquake swarms at Mount Pinatubo, Philippines: Implications for magma dynamics, *J. Volcanol. Geotherm. Res.*, *92*, 295–320.

Reid, R. C. (1978a), Superheated liquids: A laboratory curiosity and, possibly, an industrial curse. Part 1: Laboratory studies and theory, *Chem. Eng. Educ.*, *12*, 60–63, 83.

Reid, R. C. (1978b), Superheated liquids: A laboratory curiosity and, possibly, an industrial curse. Part 2: Industrial and vapor explosions, *Chem. Eng. Educ.*, *12*, 108–111, 127–129.

Reid, R. C. (1978c), Superheated liquids: A laboratory curiosity and, possibly, an industrial curse. Part 3: Discussion and conclusions, *Chem. Eng. Educ.*, *12*, 194–196, 203–206.

Reid, R. C. (1979), Possible mechanism for pressurized-liquid tank explosions or BLEVE's, *Science*, *203*, 1263–1265.

Rice, J. A. (1995), *Mathematical Statistics and Data Analysis*, 2nd ed., Duxbury, Belmont, Calif.

Scholz, C. H. (2002), *The Mechanics of Earthquakes and Faulting*, 2nd ed., Cambridge Univ. Press, Cambridge, U. K.

Scott, W. E., D. R. Sherrod, and C. A. Gardner (2008), Overview of the 2004–2006, and continuing, eruption of Mount St. Helens, Washington, in *A Volcano Rekindled: The Renewed Eruption of Mount St. Helens, 2004–2006*, edited by D. R. Sherrod, W. E. Scott, and P. H. Stauffer, *Prof. Paper 1750*, chap. 1, pp. 3–22, U.S. Geol. Surv., Reston, Va.

Shevenell, L., and F. Goff (1993), Addition of magmatic volatiles into the hot spring waters of Loowit Canyon, Mount St. Helens, Washington, USA, *Bull. Volcanol.*, *55*, 489–503.

Stephens, C. D., and B. A. Chouet (2001), Evolution of the December 14, 1989 precursory long-period event swarm at Redoubt Volcano, Alaska, *J. Volcanol. Geotherm. Res.*, *109*, 133–148.

Thelen, W. A., R. S. Crosson, and K. C. Creager (2008), Absolute and relative locations of earthquakes at Mount St. Helens, Washington using continuous data: Implications for magmatic processes, in *A Volcano Rekindled: The Renewed Eruption of Mount St. Helens, 2004–2006*, edited by D. R. Sherrod, W. E. Scott, and P. H. Stauffer, *Prof. Paper 1750*, chap. 4, pp. 71–95, U.S. Geol. Surv., Reston, Va.

Thiéry, R., and L. Mercury (2009a), Explosive properties of water in volcanic and hydrothermal systems, *J. Geophys. Res.*, *114*, B05205, doi:10.1029/2008JB005742.

Thiéry, R., and L. Mercury (2009b), Explosive conditions of aqueous solutions, *J. Solution Chem.*, *38*, 893–905.

Tong, L. S., and Y. S. Tang (1997), *Boiling Heat Transfer and Two-Phase Flow*, *Ser. Chem. Mech. Eng.*, 2nd ed., Taylor and Francis, Washington, D. C.

Tuffen, H., and D. Dingwell (2005), Fault textures in volcanic conduits: Evidence for seismic trigger mechanisms during silicic eruptions, *Bull. Volcanol.*, *67*, 370–387.

Wagner, W., and A. Pruss (2002), The IAPWS formulation 1995 for the thermodynamic properties of ordinary water substance for general and scientific use, *J. Phys. Chem. Ref. Data*, *31*(2), 387–535.

Waite, G. P., B. A. Chouet, and P. B. Dawson (2008), Eruption dynamics at Mount St. Helens imaged from broadband seismic waveforms: Interaction of the shallow magmatic and hydrothermal systems, *J. Geophys. Res.*, *113*, B02305, doi:10.1029/2007JB005259.

Wohletz, K. H. (1986), Explosive magma-water interactions: Thermodynamics, explosion mechanisms, and field studies, *Bull. Volcanol.*, *48*, 245–264.

Zimanowski, B., G. Frohlich, and V. Lorenz (1991), Quantitative experiments on phreatomagmatic explosions, *J. Volcanol. Geotherm. Res.*, *48*, 341–358.

B. A. Chouet, U.S. Geological Survey, 345 Middlefield Rd., MS 910, Menlo Park, CA 94025, USA.

R. S. Matoza, CEA/DAM/DIF, F-91297 Arpajon, France. (robin.matoza@cea.fr)